



HAL
open science

Altering the Temporal Regulation of One Transcription Factor Drives Evolutionary Trade-Offs between Head Sensory Organs

Ariane Ramaekers, Annelies Claeys, Martin Kapun, Emmanuele Mouchel-Vielh, Delphine Potier, Simon Weinberger, Nicola Grillenzoni, Delphine Dardalhon-Cumenal, Jiekun Yan, Reinhard Wolf, et al.

► **To cite this version:**

Ariane Ramaekers, Annelies Claeys, Martin Kapun, Emmanuele Mouchel-Vielh, Delphine Potier, et al. Altering the Temporal Regulation of One Transcription Factor Drives Evolutionary Trade-Offs between Head Sensory Organs. *Developmental Cell*, 2019, 50 (6), pp.780+. 10.1016/j.devcel.2019.07.027 . hal-02359426

HAL Id: hal-02359426

<https://hal.science/hal-02359426>

Submitted on 20 Jul 2022

HAL is a multi-disciplinary open access archive for the deposit and dissemination of scientific research documents, whether they are published or not. The documents may come from teaching and research institutions in France or abroad, or from public or private research centers.

L'archive ouverte pluridisciplinaire **HAL**, est destinée au dépôt et à la diffusion de documents scientifiques de niveau recherche, publiés ou non, émanant des établissements d'enseignement et de recherche français ou étrangers, des laboratoires publics ou privés.



Distributed under a Creative Commons Attribution - NonCommercial 4.0 International License

Altering the temporal regulation of one transcription factor drives evolutionary trade-offs between head sensory organs

Ariane Ramaekers^{1*†}, Annelies Claeys^{2,3}, Martin Kapun^{4‡}, Emmanuèle Mouchel-Vielh⁵, Delphine Potier⁶, Simon Weinberger^{2,3}, Nicola Grillenzoni¹, Delphine Dardalhon-Cuménal⁵, Jiekun Jan^{2,3}, Reinhard Wolf⁷, Thomas Flatt⁴, Erich Buchner⁸, Bassem A. Hassan^{1,9*}

Affiliations:

1: Institut du Cerveau et de la Moelle Epinière (ICM) - Hôpital Pitié-Salpêtrière, Sorbonne Université, Inserm, CNRS, Paris, France.

2: VIB Center for Brain and Disease, VIB, Leuven, Belgium.

3: Center for Human Genetics, University of Leuven School of Medicine, Leuven, Belgium.

4: Department of Biology; University of Fribourg; Fribourg; Switzerland

5: Sorbonne Université, CNRS, Laboratoire de Biologie du Développement -Institut de Biologie Paris Seine (LBD-IBPS), Paris, France.

6: Aix-Marseille Université, CNRS, INSERM, CIML, Marseille, France.

7: Rudolf Virchow Center for Experimental Biomedicine; University of Würzburg; Würzburg; Germany

8: Institute for Clinical Neurobiology; University Hospital Würzburg; Würzburg; Germany.

9: Lead Contact

† Current affiliation: Institut Curie, PSL Research University, CNRS, Sorbonne Université, Nuclear Dynamics Laboratory, Paris, France.

‡Current affiliation: Department of Cell & Developmental Biology, Medical University of Vienna, Austria; Department of Evolutionary Biology and Environmental Studies, University of Zürich, Switzerland

* Correspondence to:

ariane.ramaekers@curie.fr

bassem.hassan@icm-institute.org

SUMMARY

Size trade-offs of visual versus olfactory organs is a pervasive feature of animal evolution. This could result from genetic or functional constraints. We demonstrate that head sensory organ size trade-offs in *Drosophila* are genetically encoded and arise through differential subdivision of the head primordium into visual versus non-visual fields. We discover that changes in the temporal regulation of the highly-conserved *eyeless/Pax6* gene expression during development is a conserved mechanism for sensory trade-offs within and between *Drosophila* species. We identify a natural single nucleotide polymorphism in the *cis*-regulatory region of *eyeless* in a binding site of its repressor Cut that is sufficient to alter its temporal regulation and eye size. Because *eyeless/Pax6* is a conserved regulator of head sensory placode subdivision, we propose that its temporal regulation is key to define the relative size of head sensory organs.

Keywords: Sensory trade-offs, Eye size, sensory development, temporal regulation, non-coding SNP, Eyeless/Pax6, Cut, Transcription factor, *Drosophila*, Evolution

INTRODUCTION

The senses animals rely on have been shaped during evolution to better navigate and exploit the environment. As a result, even closely related species living in different ecological niches show variation in the sizes and shapes of their sensory structures. Adaptive variation in visual sensory organs is a fascinating case in point and ranges from almost complete loss of the eyes in darkness-adapted animals (Partha et al., 2017; Retaux and Casane, 2013) to the expansion of visual organs and processing areas in some other groups such as tree-dwelling mammals (Campi et al., 2011; Campi and Krubitzer, 2010) and predator insects (Elzinga, 2003). A striking, yet poorly understood feature of natural variation in eye size is that it often occurs as a trade-off between the visual organs and other head sensory structures such as olfactory organs. This was described in a large variety of animal groups including mammals (Nummela et al., 2013), and fishes (Retaux and Casane, 2013). In arthropods as well, trade-offs between the size of the eyes and of the antennae, where most olfactory organs are located, are pervasive. Examples include beetle species with different life-styles (nocturnal *vs* diurnal; visual hunters or not; (Bauer and Kredler, 1993); fireflies emitting or not emitting light signals (Stanger-Hall et al., 2018); surface and cave crustaceans (Protas and Jeffery, 2012) and millipedes (Liu et al., 2017). This is also the case between and within species of fruit flies, in which eye size often anti-correlates with the size of the face and/or of the antennae (Arif et al., 2013; Gaspar et al., 2019; Keesey et al., 2019; Norry and Gomez, 2017; Posnien et al., 2012). However, the developmental mechanisms that govern such trade-offs are essentially unknown.

A commonly observed property of sensory organ formation is the shared developmental origin of most head sensory structures – such as eyes and noses – that derive from the subdivision of a single multipotent primordium. In vertebrates, the olfactory and lens placodes

derive from the subdivision of the anterior aspect of a multipotent preplacodal ectoderm (Grocott et al., 2012; Singh and Groves, 2016). Similarly, during *Drosophila* development, the ectodermal eye-antennal imaginal disc (EAD) gives rise to all external sensory, including the visual (compound eyes and ocelli) and olfactory (antennae and maxillary palps) sense organs, and non-sensory head cuticle. In vertebrates and in flies, antagonistic relationships between gene regulatory networks (GRNs) and signaling pathways that promote different sensory identities regulate the subdivision of the multipotent primordium (Grocott et al., 2012; Singh and Groves, 2016; Wang and Sun, 2012; Weasner and Kumar, 2013). First active in the entire tissue, their expression segregates as the visual and non-visual territories become distinct (Bhattacharyya et al., 2004);(Kenyon et al., 2003). In addition to promoting eye fate, the transcription factor (TF) Pax6 and its two *Drosophila* orthologues Eyeless (Ey) and Twin-of-Eyeless (Toy), play a key role in the growth and the subdivision of the multipotent primordium (Zhu et al., 2017). In *Drosophila*, at early developmental stages, Ey and Toy are co-expressed in the entire EAD with antennal TFs, such as Homothorax (Hth). The expression of these eye and antenna-promoting TFs progressively segregates along the EAD's anterior-posterior axis, delineating the posterior eye and anterior antennal compartments. Eye and antennal TFs mutually repress each other: the antennal TFs Hth and Cut (Ct) directly repress *ey* expression while Sine oculis, another eye promoting TF, represses *ct* (Anderson et al., 2012; Wang and Sun, 2012; Weasner and Kumar, 2013). Consequently, loss or gain of function of these selector TFs leads to the transformation of most of the head tissue into visual or olfactory organs at the expense of the other sensory structure (e.g. (Anderson et al., 2012; Czerny et al., 1999; Halder et al., 1995)).

Therefore, the subdivision of a single multipotent primordium into distinct territories through mutual repression by antagonistic TFs is a shared step of the development of head

sensory organs across animals. It is thus tempting to speculate that evolutionary mechanisms have exploited this process leading to natural sensory size trade-offs between visual and olfactory organs. A hint in that direction comes from studies on *Astyanax* fishes, which live as cave or surface-dwelling morphs (Retaux and Casane, 2013). Cave morphs have small lenses and large olfactory placodes, while surface-dwellers show the reciprocal ratio. Chemical manipulation of signaling pathways that regulate the subdivision of the lens versus olfactory territories mimics the differences observed between natural morphs (Hinaux et al., 2016). Whether this is a mechanism of natural variation in sensory trade-offs is unknown. Demonstrating a direct link requires the identification of naturally occurring causal genetic variants and the elucidation of their effect on the GRNs that regulate visual and olfactory sensory organ development. The paucity of model systems amenable to combining comparative, genetic, molecular and developmental analyses has thus far hindered such an endeavor.

We reasoned that natural variation in eye size between and within *Drosophila* species may offer precisely such a model. We therefore used comparative analyses combined with developmental, molecular and genome editing approaches to tackle this question. We show that differential subdivision of the EAD, resulting in different proportions of eye and antennal compartments, underlies eye size variation between and within *Drosophila* species. In both cases, this is associated with changes in the temporal regulation of the expression of *ey* during EAD subdivision. We also demonstrate that in *D. melanogaster* (*D. mel.*), this is caused by a non-coding single polymorphic nucleotide (SNP) present in most natural populations of *D. mel.* This SNP is located in a binding site for the antennal factor Ct within the eye enhancer of *ey*. Using CRISPR/Cas 9 genome editing, we show that this SNP is causal to temporal changes in *ey* expression and to facet number variation. Thus, changes in the subdivision of a multipotent

primordium, caused by subtle alterations of the mutual repression between distinct fates, underlies natural variation in sensory trade-offs.

RESULTS

Reciprocal changes in the sizes of visual and non-visual head structures

The insect compound eye is composed of a crystalline array of small units, named facets or ommatidia. In insects, and specifically in Drosophilids, eye size depends both on the number and diameter of the ommatidia and is often negatively correlated with face and/or antenna size (Arif et al., 2013; Norry and Gomez, 2017; Posnien et al., 2012) (Gaspar et al., 2019; Keesey et al., 2019). In this study, we selected four *Drosophila* species, which presented a larger eye to face width ratio as compared to *D. mel.* (Figure 1A-1A'; Figure S1). All subsequent morphological measurements were performed on females raised in density-controlled conditions. We focused on *Drosophila pseudoobscura* (*D. pse.*), which had the largest difference in terms of ommatidia number, an increase of 35% as compared to *D. mel.* (Figures 1B and 1B') while sharing similar facet diameters (Figures 1C and 1C'). Interestingly, the third antennal segment, which hosts the olfactory sensillae, was thinner in *D. pse.* as compared to *D. mel.* (Figures 1D and 1E). As a control, we measured tibia length as a proxy to body size (Arif et al., 2013; Posnien et al., 2012) (Figure S2). In line with previous studies e. g. (Arif et al., 2013; Gaspar et al., 2019; Keesey et al., 2019; Posnien et al., 2012), our results suggest that variation in eye, face or antennal size cannot be explained solely by variation in body size.

Increased facet number has been associated with higher visual acuity in predator flies (Elzinga, 2003; Gonzalez-Bellido et al., 2011). We thus tested whether a modest variation such as the one observed between *D. pse.* and *D. mel.* was potentially relevant to visual function. We

measured the minimal angular distance between two successive vertical black stripes resolved by the flies as a read-out of their visual acuity (Figure 1F) (Buchner, 1976; Gotz, 1964). *D. pse.* were able to distinguish between more closely juxtaposed stripes (minimal angle = 7.0°) as compared to *D. mel.* (minimal angle = 8.51°) (Figure 1F'). Thus, *D. pse.* have a better visual acuity correlating with an increased number of facets.

A trade-off between eye and non-eye progenitor fields

What is the developmental origin of facet number variation between *D. mel.* and *D. pse.* and why does it inversely correlate with the size of non-visual structures? All external structures of the head of the adult fly including the sensory organs develop from the EAD (Figure 2A). The eye field occupies most of the posterior EAD compartment and is marked by the expression of Eyes Absent (Eya; Figure 2B) (Roignant and Treisman, 2009). We measured the surface of the eye field in late, fully-grown, EADs (stage P0) using Eya and found that the eye field was 31% larger in *D. pse.* than in *D. mel.* (Figure 2B'). This is very close to the 35% difference in the number of adult eye facets. We therefore queried the developmental origin of the difference in eye field size between the two species and considered several possibilities. A first possibility is that the initial pool of embryonic cells forming the EAD differs between the two species. In the late embryo (stage 17), the EADs is composed of a few dozen closely juxtaposed cells located anterior to the brain. Using Ey as a marker, we quantified and compared the number of embryonic EAD cells between the two species (Figures 2D and 2D') but found no significant difference in the number of EAD progenitors, ruling out this first possibility. Variation in eye field size could also originate from different rates of proliferation. However, the similar density of mitotic cells in the proliferating eye field in EADs of the two species did not support this hypothesis (Figures 2F and 2F'). In addition, the density of ommatidia progenitor cells in the eye

field, characterized by the expression of the proneural factor Atonal, was similar between the two species (Figures S3A-S3A’). Finally, variation in eye field size could also derive from a change in the subdivision of the EAD between eye and non-eye fields. To test this possibility, we compared the proportion of the EAD occupied by the eye field in early L3 imaginal discs, after the subdivision between the fields is completed (Figure 2E). The total EAD size was similar between the two species, confirming that it underwent similar growth during prior larval development (Figure 2E’). In contrast, already at this early stage, the eye field was proportionally larger in *D. pse.* than in *D. mel.* (Figure 2E’). Thus, the two species differ by the proportion of the multipotent EAD dedicated to the eye versus non-eye tissues, resulting in different proportions of the head structures in the adult. Therefore, the species variation in eye size involves a developmental trade-off between eye and non-eye primordia.

Temporal regulation of EAD subdivision governs the trade-off between eye and non-eye fields

What are the regulatory mechanisms governing this developmental trade-off? EAD subdivision requires the temporally progressive restriction of selector TFs expression to the anterior ‘antennal’ or posterior ‘eye’ compartments, a process completed by mid to late second instar larval stage (L2) (Kenyon et al., 2003). At this developmental time point, the mutually exclusive expression domains of antenna and eye selectors define the relative sizes of the compartments. In *D. mel.*, a 3.2 kb *cis*-regulatory intron governs *ey* expression during eye development (Figure 3A). We cloned the orthologous intron from *D. pse.* based on the conservation of the flanking exons. The *D. pse.* intronic sequence is slightly shorter (3.0 kb) with 22% of the intron from *D. mel.* aligning to the corresponding sequences in *D. pse.* (Figure 3B). Nonetheless, when inserted at the same position in *D. mel.* genome, both *D. mel.* and *D. pse.*

introns were able to drive GFP expression in the EAD throughout eye development, revealing global functional conservation (not shown).

We tested whether, despite their overall functional conservation, subtle changes in *ey* regulation exist between *D. mel.* and *D. pse.* introns (Figures 3C-3D'). In early EADs (late embryos and in L1), both *D. mel.* and *D. pse.* enhancers drove GFP expression across the entire disc (Figure S4). At the L2 stage, we noted that GFP expression driven by the *melanogaster* enhancer (*D.m.ey3.5*) (Figures 3C and 3C') extended further anteriorly into the antennal compartment as compared to the *pseudoobscura* enhancer (*D.p. ey3.3*) (Figures 3D and 3D'). This means that the posterior retraction of expression driven by the two *ey* enhancers occurs at different velocities. To quantify this effect, we generated two lines of transgenic *D. mel.* flies. The first line carries two transgenes driving the expression of the red fluorescent protein mCherry and of the green fluorescent protein (GFP), respectively, both under the control of *D. mel. ey* enhancer. In this control line, any difference in the expression of mCherry and GFP driven by the same enhancer must only be caused by different dynamics of the two fluorescent proteins. In the second line, mCherry was driven by the *D. mel. ey* enhancer, while GFP was driven by *D. pse. ey* enhancer. In this case, the differences in expression between the GFP and mCherry is caused both by different dynamics of the fluorescent proteins as well as differences in their transcriptional regulation. Thus, to detect differences in the activity of *D. mel.* and *D. pse. ey* enhancers, we performed pairwise comparisons of the difference between GFP and mCherry expression in line 1 versus line 2. In early L3 discs, when the antennal and eye compartments have already segregated, the co-expression of mCherry and GFP driven by either *D. mel.* or *D. pse.* regulatory sequences were indistinguishable (Figures 3F and 3F'). In contrast, at L2, during the process of *ey* retraction, the posterior retraction of the GFP was more

posteriorly advanced when driven by the *D. pse.* than by the *D. mel.* enhancer (Figures 3E and 3E’). Therefore, the partitioning of the EAD into eye and non-eye fields occurs at an earlier time point in *D. pse.* compared to *D. mel.* Since Ey positive cells proliferate more than Ey negative cells (Zhu et al., 2017), earlier establishment of the two sensory fields would drive greater differential growth.

A conserved mechanism of sensory trade-offs

To understand the genetic basis of sensory trade-off in *Drosophila*, we exploited the fact such trade-offs have also been observed within single fly species (Arif et al., 2013; Cowley and Atchley, 1990; Gaspar et al., 2019; Norry and Gomez, 2017; Posnien et al., 2012). We found that two wild-type *D. mel.* laboratory strains, Canton-S and Hikone-AS, show different eye-to-face ratios. This is associated with changes in ommatidia number (12, 5 % more facets in Canton-S) and diameter (Figures 4A and 4B, Figures S1A - S1D, Table 1) as well as variation of antennal width (Figure 4C). F1 progeny of Canton-S and Hikone-AS parents presented intermediate ommatidia numbers relative to their parents, demonstrating the heritable nature of this trait (Figure 4D). We asked if facet number variation between Canton-S and Hikone-AS also originate from changes in the subdivision of the EAD into eye versus non-eye territories. We compared the subdivision of early L3 EADs between the two strains. While the size of the entire EAD was unchanged, the eye field was proportionally larger in Canton-S than in Hikone-AS (Figures 2E – 2E’). These data suggest that, despite 17 - 30 million years of separated evolution between the two species groups (Obbard et al., 2012), ommatidia number variation between *D. mel.* and *D. pse.* and between two *D. mel.* strains, shares a common developmental logic.

A single nucleotide in a Ct binding site distinguishes the Canton-S and Hikone-AS *ey* regulatory sequences

Does the difference in EAD subdivision between the Canton-S and Hikone-AS also result from a differential temporal regulation of *ey*? To answer this question, we cloned and aligned the *ey cis*-regulatory sequence from the Canton-S and Hikone-AS strains (Figure 4D). In contrast to the significant divergence observed between *D. mel.* and *D. pse.*, Hikone-AS and Canton-S intron sequences were nearly identical and differed only by a single nucleotide over the entire 3.2 kb intronic region, a G>A substitution at position chr4: 710326. *In silico* analyses revealed that this single nucleotide variant (SNV) is located in a Ct binding site, distinct from the three sites previously described in the *ey cis*-regulatory sequence (Figure 4E) (Wang and Sun, 2012). Interestingly, the two variants are predicted to display different affinities for the repressor, in a manner that anti-correlates with the number of ommatidia: the A-allele presents a lower affinity score (4.56) and is associated with larger eyes (Canton-S) as compared to the G-allele (Hikone-AS; predicted affinity score 5.22) (Figure 4E' and Figure S4). We thus performed electrophoretic mobility shift assays using a tagged recombinant Ct protein (Figure 4F), and found that Ct has the ability to bind to this sequence. Next, we tested the affinities of the two sequences by performing a competition assay in which unlabeled A-probes or unlabeled G-probes competed with the labeled G-probe. While unlabeled G-probes effectively suppressed the shift, the unlabeled A-probes did not, providing biochemical evidence that the two variants have different affinities for Ct. Put together, these results suggest that the strength of *ey* repression by Ct, a selector TF for antennal fate and a repressor of *ey* expression, influence eye size (Wang and Sun, 2012; Weasner and Kumar, 2013). Consistent with this, RNAi knock-down of *ct* expression during EAD development was sufficient to increase facet number in the adult eye (Figure 4G,

Figure S5). We note however that this did not consistently result in antagonistic trends in face and antennal width, possibly due to pleiotropic effects of *ct* loss-of-function on head development (Figure S5).

These findings raise two questions: first, is the *G* to *A* substitution in the *ey* *cis*-regulatory sequence sufficient to cause temporal changes in its activity; and second, if so, might such changes be caused by alterations in the regulation of the *ey* enhancer by Ct? To tackle these two questions, we used the same strategy described above for comparing the *D. pse.* and *D. mel.* enhancers using GFP and mCherry reporters. We first compared the activities of the Canton-S (*A*-allele) and the Hikone-AS (*G*-allele) of the *ey* 3.5 *cis*-regulatory sequences. At early/mid L2, during EAD subdivision, mCherry and GFP co-expression differed between the alleles such that the *A*-carrying variant (Canton-S; larger eyes) showed further posterior retraction of GFP expression than the *G*-carrying variant (Hikone-AS; smaller eyes) (Figure 4H-4H'). In contrast, at early L3, after EAD subdivision is completed, the two alleles drove similar expression of GFP and mCherry (Figure 4I-4I').

Could this differential temporal retraction of the *ey* enhancer be caused by changes in *ey* repression by Ct? To test this, we created two new synthetic *ey* enhancers, based on *in silico* predictions (Figure 4E'). The first, which we call the *NoCt* variant, is predicted to abolish Ct binding to the site harboring the *G/A* SNP (predicted affinity score <3). The second, which we call *ConsensusCt*, creates a Ct consensus-binding motif at that position (predicted affinity score 6.62). Remarkably, the *ConsensusCt* variant behaved similarly to the *G*-allele, while the *NoCt* variant mimicked the *A*-allele in that it caused faster posterior retraction of *ey* enhancer activity (Figure 4H-I'). This further suggests that the Canton-S *A*-allele may constitute a lower affinity site for the Ct repressor as compared to the Hikone-AS *G*-allele.

Thus far, we showed that the changes in EAD subdivision between Hikone-AS and Canton-S and between *D. mel.* and *D. pse.* are both driven by differential temporal dynamics of the posterior retraction of *ey* expression. Within the *D. mel.* this is associated with a SNV in *ey* eye enhancer, which introduces subtle changes in *ey* regulation, by affecting its repression by the antennal selector TF Ct.

A common SNP in *D. mel.* natural populations is associated with facet number variation

Because Hikone-AS and Canton-S flies have been in artificial lab culture conditions for decades, we asked if either of these two alleles is found in natural fruit fly populations. By investigating allele frequency patterns in whole-genome data of worldwide population samples, we found that most natural populations from Europe, North America, Asia and Australia are polymorphic at this position. Thus, neither of the two alleles corresponds to a *de novo* mutation and variation at this position corresponds to a relatively frequent SNP (Figures 5A and A'; Table S2). Populations from Sub-Saharan Africa are mostly fixed for the *G*-allele suggesting that the *A*-allele is a derived variant that appeared after *D. mel.* left Africa and colonized the rest of world. In line with this hypothesis, we found statistical evidence (FET test, $p=0.02$) that the few African populations carrying the *A*-variant are more likely to be admixed with European genetic variation than the ones with the putatively ancestral *G*-allele (Table S3). Moreover, the frequency of the *A*-variant decreased from West to East in European populations (Figure 5A' and 5B). The slope of the longitudinal frequency cline of the *ey* SNP deviated significantly from that of 21,008 genome-wide SNPs in short introns that presumably evolved neutrally (Figure 5C), suggesting that the clinal pattern is not solely the result of neutral evolution or demography (see also Figure S7).

Causal effect of the SNP on eye size

We further noted that natural populations from North-East America, where the Canton-S strain originated, are highly polymorphic for the *ey* SNP (Figure 5A, Table S2). By comparing Canton-S flies from three laboratories, we discovered that, while our Canton-S lab isolate (henceforth Canton-S^{BH}) carries the A-allele, two other strains from two different laboratories in Paris, France (T. Pr at) and Florida, USA (R. Davis) were homozygous for the G-allele, similar to Hikone-AS. This strongly suggests that the original Canton-S population was polymorphic and that the two alleles were eventually segregated during the separate maintenance of different laboratory stocks (Colomb and Brembs, 2014). This provided a unique opportunity to quantify the contribution of the G/A SNP to eye size in a relatively homogenous background. By comparing ommatidia numbers between the three stocks, we observed that Canton S^{BH} flies have significantly more facets than its two siblings (Figure 6A, Table 1), a difference that anti-correlates with their face and antennal width (Figure S6). These data suggest that the A-variant may be sufficient to drive larger facet numbers, possibly at the expenses of other head structures. To test this idea directly, we used CRISPR/Cas9 to introduce the A-allele in a G-homozygous stock. We recovered one transformant male carrying the A-allele and controlled that it bore no other mutation in the *ey* regulatory intron. Comparing ommatidia numbers between engineered G>A flies and the G-carrying control revealed an increase in eye size associated with the G>A substitution (Figure 6B, Table 1). It recapitulated up to 49 % of the difference between Hikone-AS and Canton-S^{BH} and up to 86% of the variation observed between Canton-S^{BH} and Canton-SRD and Canton-S^{TP}, respectively. Three other A-homozygous lines deriving from the same transformant male were established to account for subtle differences in the genetic background of the flies. The three stocks followed the same trend, i.e. an increased facet number when

compared to the *G*-homozygous controls, reaching statistical significance in two out of the three (Figure S6). This result suggests that the *ey cis*-regulatory SNP is causal to facet number variation. Next, we combined the two alleles with Df(4)J2, a large deficiency covering the entire *ey* locus. These flies recapitulated the phenotypes of the corresponding homozygous alleles, indicating that an undetected lesion outside of the *ey* locus did not cause the effect on eye size attributed to the *A*-allele (Figure 6C). In addition, in both cases, the antennae show a trend towards decreasing in size, but this trend did not reach statistical significance (Figure S6), likely due to the small size of the difference.

DISCUSSION

In 1987, Montgomery Slatkin proposed a mathematical model (Slatkin, 1987), which he referred to as “unrealistically simple”, predicting that mutations modifying the time at which “traits developing from the same tissue” begin to grow independently changes the relative size of the traits. Size trade-offs between head sensory organs represent precisely the types of traits referred to in Slatkin’s model. However, whether visual-olfactory sensory trade-offs follow a “Slatkin model” and if so, what the genetic basis of such a model are, remained unexplored.

In this study, we find that differential subdivision of the head primordium into eye and non-eye progenitor fields constitutes a developmental mechanism for creating different proportions of head structures in fruit flies, including trade-offs between the olfactory antennae and the eyes. We further demonstrate that this is associated with differential temporal regulation of the expression of the conserved eye selector transcription factor, *Ey/Pax6*. We propose a model (Figure 6D to 6F) whereby early in development, the homogenous expression of *ey*, which promotes its proliferation (Zhu et al., 2017), causes homogenous growth throughout the entire EAD. Later, the progressive retraction of *ey* expression from the anterior antennal compartment

creates an asymmetry in growth rate. Modulating the velocity of *ey* retraction through mutations affecting the bistable switch between GRNs governing antennal *vs* eye identity, changes the relative time during which the anterior and posterior compartments grow at different rates resulting in their different proportions. This provides direct biological evidence for mathematical models linking heterochrony in development to changes in adult traits (Cowley and Atchley, 1990; Riska, 1986; Slatkin, 1987). Our observation of similar changes in *ey* temporal regulation between and within species further suggests that the temporal mechanism we identify may represent a “preferred route” to relative variation in sensory organ size because it results in no dramatic “pleiotropic” effects associated with changes to growth, patterning or specification. We speculate that such variation of the temporal regulation of EAD partitioning could be caused by a variety of molecular changes acting either in *cis* or in *trans* on the GRNs governing eye and antennal compartment identities.

In this work we uncovered an example of such a molecular change to the regulation of these GRNs. Specifically, within *D. mel.*, a naturally occurring SNP in the eye-enhancer of *ey* is sufficient to modulate the velocity of the posterior retraction of the enhancer activity and to vary facet numbers in the adult eye. The SNP, a G/A substitution, is located in a binding site for *ey* repressor Ct. *In silico* predictions and EMSA experiments indicate that the G/A substitution modifies the affinity of Ct for the binding site. This suggests that different levels of *ey* repression by Ct are responsible for changing the dynamics of *ey* regulation and ultimately for causing morphological variation, a lower affinity of the binding site for Ct resulting into faster enhancer retraction and larger eyes and vice versa. This view is further supported by our findings that (i) synthetic mutations predicted to support or reduce Ct binding mimic the effect of the SNP on the velocity of the enhancer retraction; and that (ii) knocking-down Ct expression increase

compound eye size. Interestingly, the highly divergent *ey* enhancers from *D. mel.* and *D. pse.* display similar differences in regulation, i.e. a faster retraction of the enhancer of the “larger eye” species. However, what feature of the two enhancer sequences causes their different temporal regulation is not known. A recent study identified a single nucleotide insertion that influences photoreceptor specification and ultimately color preference in *Drosophila* by modulating the affinity for a TF named Klumpfuss (Anderson et al., 2017). Together with our work, this suggests a general role for variation in suboptimal TF binding sites in sensory evolution (Crocker et al., 2016).

In vertebrates, antagonistic relationships between GRNs and signaling pathways that promote different sensory identities also regulate the subdivision of the multipotent sensory placode (Grocott et al., 2012; Singh and Groves, 2016). The anterior placodal region, which gives rise to the lens and olfactory placodes, expresses *pax6*. In the absence of *pax6*, both lens and olfactory placodes fail to thicken and to develop properly (Ashery-Padan et al., 2000; Collinson et al., 2000; Quinn et al., 1996). Interestingly, the temporal regulation of the *pax6* placode enhancer is altered by manipulating suboptimal binding sites for one of its activators (Rowan et al., 2010). In addition, the *pax6* ectodermal enhancer shows evidence of accelerated evolution in subterranean mammalian species (Partha et al., 2017). This is consistent with our model whereby naturally occurring mutations that alter *pax6* regulation, either in *cis* or in *trans*, constitute a common genetic origin of the trade-offs between visual and olfactory organ size.

In “The Origin of Species”, Charles Darwin referred to the evolution of the eye as a challenge to his theory (Darwin, 1872). He also discussed the importance of correlation between body parts concluding that it was “most imperfectly understood”. During the last decades, the common origin of animal eyes and their evolution over long evolutionary distances has been

abundantly documented (Gehring, 2014). However, the developmental mechanisms by which small-scale variation in eye size or shape can take place without disrupting its organization and function remain largely elusive (Dyer et al., 2009). We have demonstrated that a single nucleotide change in a core regulator of eye development is sufficient to generate reciprocal sensory organ size variation, potentially providing a quick route to behavioural changes, and perhaps adaptation. As predicted by Darwin, adaptive variation in head derived structures, including the eye, can be produced by the accumulation of modest morphological changes, which our data suggest may be caused by a small number of genetic variants affecting the temporal regulation of core regulatory networks.

ACKNOWLEDGMENTS

This work was funded by VIB (B.A.H), the Belspo WiBrain Interuniversity Attraction Pole network and Fonds Wetenschappelijke Onderzoeks (FWO) grant G.0503.12 (B.A.H.). Work in B.A.H lab is currently funded by the Institut Hospitalier Universitaire (IHU) and the Institut du Cerveau et de la Moëlle Epinière (ICM), Paris, France. S.W. was a fellow of the FLiACT Marie Curie ITN (FP7, EU). M.K. and T.F. were supported by a Swiss National Science Foundation (SNSF) grant (PP00P3_133641) to T.F. We thank M. Lang, B. Lefèvre, S. Villain, R. Ejsmont, N. Mora, A. Soldano, N. Gompel, N. Posnien and D. Nunes for advices, discussion or/and technical help; J. Clements and P. Callaerts for sharing reagents. We acknowledge the *Drosophila* Species Stock Center (DSSC), the Bloomington Stock Center (NIH P40OD018537), the Kyoto Stock Center (DGRC), for sending *Drosophila* stocks, the Developmental Studies Hybridoma Bank (DHSN, University of Iowa) for sending antibodies and Addgene for sending plasmids. We are grateful to P. Baatsen from the Electronic Microscopy Platform for support with SEM sample preparation and imaging. Confocal imaging was

performed at the VIB Light Microscopy and Imaging Network (Limone) and at the Plateforme d'imagerie cellulaire (PICPS) at the ICM. The Leica TCS Sp5 II confocal microscope and the Nikon were acquired respectively by the VIB BioImaging Core and through a Hercules type 1 grant (AKUL/09/037) to W. Annaert. B.A.H. is an Allen Distinguished Investigator and an Einstein Visiting Fellow of the Berlin Institute of Health.

AUTHOR CONTRIBUTIONS

A.R. conceived the project. A.R. and B.A.H. designed the experiments. A.R. and J.Y. acquired SEM and light microscopy images. A.R., N.G. and S.W. performed and imaged immunostainings on imaginal discs, A.R. and N.G. quantified and analyzed the imaging data. A.R. and A.C. generated the constructs and performed allele-specific PCR. J.Y. injected the CRISPR constructs. E.B. and R.W. performed and analyzed the optomotor tests. M. K. and T. F. performed population genetics analyses. D. P. performed Ct binding sites *in silico* predictions and synthetic enhancers design. D. C. and E. M. V. performed the EMSAs. A.R. and B.A.H. wrote the manuscript.

DECLARATION OF INTERESTS

The authors declare no competing interests.

FIGURE LEGENDS

Figure 1. Natural variation in *Drosophila* facet number, see also Figure S1

(A to C') Eye size comparisons between the *D. mel.* (*D. mel.*) and *D. pse.* (*D.pse.*). Boxes indicate interquartile ranges, lines medians and whiskers data ranges. Scale bar for (A) and (B), 100 μm ; for (C), 10 μm .

(A and A') Ratio between eye (E) and face (F) width. Sample sizes: *D. mel.* (n=23), *D. pse.* (n=26). Two-tailed unpaired t-test: **** $p < 0.0001$.

(B and B') Ommatidia number. Sample sizes: *D. mel.* (n=9), *D. pse.* (n=8). Two-tailed unpaired t-test: **** $p < 0.0001$.

(C and C') Ommatidia width. Sample size: n=24. Two-tailed unpaired t-test with Welch's correction: *n.s.* $p = 0.1677$.

(A and D) Third antennal segment (A3) width. Sample sizes: n=5. Two-tailed unpaired t-test: * $p = 0.0409$

(E) Optomotor response set-up (*see* Materials and Methods).

(E') Optomotor response (normalized to max) of *D. mel.* and *D. pse.* females in function of stripe width (spatial wavelength λ); (mean \pm sem). Arrows: spatial resolution (measured as the zero-crossing angle $2\Delta\Phi$). Sample size: n=9. Two-tailed unpaired t-test: * $p = 0.014$.

Figure 2. Developmental origin of eye size variation in *D. mel.* and *D. pse.*, *see also* Figure S3

(A) Schematics of the distinct fields of the EAD giving rise to the adult sensory and non-sensory head structures (Ant, antenna; MxP, maxillary palps; Oc, ocelli). Anterior is at the left.

(B) Late L3 EAD from *D. pse.*. The eye field (yellow dashed line) is labelled with anti-eya (red) and committed photoreceptors are shown in yellow (anti-elav); blue: DAPI. Anterior is at the left. Scale bar: 50 μm .

(B') Eye field surface in late (P0) eye-antennal discs. Sample sizes: *D. mel.* (n=19); *D. pse.* (n=19). Two-tailed unpaired t-test with Welch's correction **** $p < 0.0001$.

(C) Schematics of eye-antennal disc development. Insets: (C') segregation of "antennal" and "eye" compartments during L2; (C'') determination of ommatidia precursor cells during L3.

(D) Dorsal view of a late Canton-S embryo depicting the Ey-positive EADs (yellow dashed line) flanking the brain (white dashed line). Anterior is at the top. Scale bar: 25 μm .

(D') Cell content of late embryonic EADs. Sample sizes: *D. mel.* (n=22); *D. pse.* (n=33). Two-tailed unpaired t test; *n. s.* $p=0.0959$.

(E) Early L3 Canton-S EAD co-labelled by Eya (yellow dashed line) and Ct (asterisk). Anterior is at the left. Scale bar: 25 μm .

(E') Total surface of the EADs (in μm^2). Ordinary one-way ANOVA ($p=0.4520$) followed by Dunnett's multiple comparisons tests.

(E'') Ratio of eye field vs total EAD surface. Ordinary one-way ANOVA ($p<0.0001$) followed by Dunnett's multiple comparisons tests. Sample sizes: CS (n=11); Hik (n=9); Cat (n=8).

(F). Proliferative portion of the eye field (dashed yellow line). Red: eye field (anti-Eya); Green: mitotic cells (anti-phosphorylated Histone 3). Anterior is at the left. Scale bar: 25 μm .

(F') Mitotic index of the proliferative eye field in *D. mel.* and *D. pse.* early L3 EADs. Sample sizes: *D. mel.* (n=20); *D. pse.* (n=8). Two-tailed unpaired t-test *n.s.* $p=0.6185$.

Boxes indicate interquartile ranges, lines medians and whiskers data ranges in all charts (B', D', E', F').

Figure 3. Different temporal regulation of EAD subdivision governs the trade-off between eye and non-eye fields

(A) Structure of the *ey* locus showing the location of the intronic *ey*^{3.5} eye enhancer (Hauck et al., 1999). E2: exon 2; E3: exon 3.

(B) Alignment of the *ey* eye enhancer between *D. mel.* and *D. pse.*. Dark grey boxes represent the fragments of the *D.mel.* intron sequence that aligned with the orthologous region of *D. pse.* using BLAST.

(C to D') GFP expression driven by *D. mel. ey3.5* and *D. pse.ey3.3* eye enhancers in mid-L2 EADs counterstained with anti-Cut. *Green*: GFP; *magenta*: anti-Cut. Yellow arrows indicate the anterior limit of GFP expression. Scale bars: 20 μ m. Anterior is at the bottom.

(E and F) Schematics and immunostainings showing ongoing (E, early / mid-L2 stage) and full (F, early L3 stage) posterior retraction of *ey* enhancer activity during EAD development.

(E' and F') Pairwise comparison of the difference in expression between GFP and mCherry, measured as the proportion of mCherry that was not colocalized with GFP, when driven by distinct combinations of *ey* eye enhancers during (E', early/mid-L2 stage) and after (F', early L3 stage) posterior retraction of *ey* enhancer activity. (*D.m.ey3.5*, *D. mel. ey* enhancer; *D.p.ey3.3*, *D. pse.* enhancer).

(E') Early/Mid-L2 stage. Sample sizes (n=8, n=12). Two-tailed unpaired t-test *** $p=0.0001$.

(D') Early-L3 stage. Sample sizes (n=10, n=3). Mann-Whitney test *n.s.* $p=0.6643$.

Figure 4. Developmental and regulatory origin of intraspecific eye size variation.

(A) Eye vs face width ratio in Canton-S (CS) and Hikone-AS (Hik). Sample sizes: CS: n=15, Hik: n=16. Ordinary one-way ANOVA **** $p<0.0001$ followed by Tukey's multiple comparisons: **** $p<0.0001$. See full data set in supplement (Figure S6), see also Figure S1.

(B) Ommatidia number. Sample sizes: CS: n=15, Hik: n=16. Two-tailed unpaired t-test: ****
 $p < 0.0001$.

(C) Third antennal segment (A3) width. Samples sizes: n=11. Ordinary one-way ANOVA ** $p = 0.0035$ followed by Tukey's multiple comparisons. ** adjusted $p = 0.0043$. See full figure in supplement (Figure S6),

(D) Frequency distribution of ommatidia numbers in CS (n=42), Hik (n=39) and their F1 progeny (n=54).

(E) Schematics of the *D. mel. ey* eye enhancer ($ey^{3.5}$) showing the localization of the $G > A$ substitution (chr4: 710326) and of three published Ct binding-sites (C, blue lines) (Wang and Sun, 2012).

(E') The dashed red rectangle delineates the low-affinity putative Ct binding site overlapping the position of the $G > A$ substitution (chr4: 710326) (Zhu et al., 2011). For each natural or synthetic enhancer allele, the best score of the Ct binding site as predicted by Cluster-Buster (Frith et al., 2003) is plotted. See also Figure S5 and Table S2.

(F) Electrophoretic Mobility Shift assay. The Cut-FLAG expressing nuclear extract elicits a bandshift when incubated with the G -Probe (black arrow). Excess unlabeled G -probe, but not A -probe effectively competes with the binding, suggesting a higher affinity of Ct for the former. Incubation with an anti-FLAG induces a supershift (empty arrowhead). Grey arrow: non-specific binding.

(G) Ommatidia number variation following RNAi-mediated knock-down of *ct*. Sample sizes from left to right (n=13; n=23; n=10; n=8). Ordinary one-way ANOVA **** $p < 0.0001$ followed by Sidak's multiple comparisons: **** $p < 0.0001$, * $p = 0.0126$. See also Figure S5.

(H to I') Pairwise comparison of the expression of the four *D. mel. ey* enhancer alleles: *ey3.5^G* (Hikone-AS); *ey3.5^A* (Canton-S); *ey3.5^{CC}* (ConsensusCt); *ey3.5^{NC}* (NoCt).

(G and H) Schematics and immunostainings of EADs with ongoing (F, early/mid-L2 stage) and full (G, early L3 stage) posterior retraction of *ey* enhancer activity.

(G' and H') Pairwise comparison of the difference in expression between GFP and mCherry, measured as the proportion of mCherry that was not colocalized with GFP, when driven by distinct combinations of *ey* eye enhancers during (F', early/mid-L2 stage) and after (G', early L3 stage) posterior retraction of *ey* enhancer activity. *ey* enhancer variants: *ey3.5^G*, *G*-variant (Hikone-AS); *ey3.5^A*, *A*-variant (Canton-S); *ey3.5^{CC}*, *ConsensusCt*-variant; *ey3.5^{NC}*, *NoCt*-variant.

(G') Mid-L2 stage. Sample sizes: (n=16, n=24, n=20, n=12). Ordinary one-way ANOVA **** $p < 0.0001$ followed by Dunnett's multiple comparisons versus *ey3.5^G*: **** *adjusted p*=0.0001, *n.s. adjusted p*=0.9828; * *adjusted p* = 0.0167.

(H') Early-L3 stage. Sample sizes from left to right (n=9; n=10; n=6; n=9). Ordinary one-way ANOVA *n.s. p*=0.9652.

Figure 5. Worldwide distribution of the *G>A* substitution (chr4: 710326) in the genome of *D. mel.* natural populations. See also Figure S7.

(A) Worldwide allele frequency patterns. Frequencies of the *A*-variant are shown as red areas of the pie charts for worldwide populations with a sample-size ≥ 10 (see Tables S2 and S3 for details). The exact geographic location for each sample is indicated by a black dot.

(A') Frequency distribution of the *A*-variant in Europe revealing the longitudinal clinal distribution of the allele.

(B) Scatter plots showing allele frequencies of the A-variant along the latitudinal (left box; red regression curve) and the longitudinal axis (right box; blue regression curve) in Europe. The top-right p values show the significance from generalized linear models (GLM).

(C) The line plot shows the empirical cumulative density function (ECDF) from $-\log_{10}$ transformed p values of GLMs with longitude as the predictor variable for 21,008 neutrally evolving intronic SNPs (black curve). The vertical red line highlights the $-\log_{10} p$ value for the focal SNP ($p=8.6 \times 10^{-13}$) which is inferior to the ones of 99.69 % of the neutral SNPs, indicating that it stronger correlation with longitude. The empirical p value ($p=0.0031$) is calculated from the area confined by the p value of 4: 710326 and the tail of the ECDF.

Figure 6. The non-coding G>A SNP in ey enhancer causes facet number variation.

(A) Ommatidia numbers in three Canton-S strains with different *ey* SNP alleles (in red). Sample sizes: Canton-S^{BH} (CS-BH, n=18), Canton-S^{TP} (CS-TP, n=16), Canton-SRD (CS-RD, n=19); Kruskal Wallis test **** $p < 0.0001$ followed by Dunn's multiple comparisons: ** *adjusted* $p = 0.0041$; **** *adjusted* $p < 0.0001$; *n.s.* *adjusted* $p = 0.1180$. See also Figure S6.

(B) Ommatidia numbers in CRISPR A-variant and control G-variant homozygous fly eyes imaged by scanning electron microscopy. Sample sizes: *ey3.5^G*: n=13; *ey3.5^{G>A-1}*: n=12. Two-tailed unpaired t-test: * $p = 0.0356$. See also Figure S6.

(C) Ommatidia numbers in CRISPR A-variant and control G-variant over a deficiency covering the entire *ey* locus. Sample sizes: $n = 18$. Two-tailed unpaired t-test with Welch's correction: * $p = 0.0138$. See also Figure S6.

(A and B) Boxes indicate interquartile ranges, lines medians and whiskers data ranges.

(C to F) Model of the developmental origin of the trade-off between EAD derived structures.

(C) The subdivision of the EAD into an anterior (“antennal”) and posterior (“eye”) compartments involves a bistable switch by which GRNs promoting eye (GRNe, *in red*) and antennal (GRNa, *in blue*) identity act antagonistically by activating their own and repressing the alternative GRN’s activity.

(D) The bistable switch between the GRNa and GRNe results in the progressive segregation of the expression domains of TFs promoting eye (posterior, *in red*) versus antennal (anterior, *in blue*) fates during successive stages of EAD development. Anterior is on the left.

(E and F) Our model, inspired from Slatkin (Slatkin, 1987), proposes that different temporal dynamics of the posterior retraction of *ey*, a promotor of EAD proliferation, by changing the relative duration of uniform versus heterogeneous growth, modifies the proportion between the antennal and eye compartments. This could be caused by genetic changes affecting the dynamics of the bistable switch between GRNe and GRNa, like in the case of the *ey G>A* substitution.

TABLE 1: Ommatidia numbers. Ommatidia numbers are counted on SEM images (count) or estimated from light-microscopy images using an ellipse-based method (estimated, see Star Methods and Figure S2).

	Ommatidia nb (<i>count</i>)		Ommatidia nb (<i>estimated</i>)	
	Mean	St Dev	Mean	St Dev
Canton-S	869.8 ^a	17.96 ^a	828.0	34.00
Hikone-AS	742.4 ^a	20.17 ^a	736.0	27.09
<i>D. pse.</i>	1177 ^a	28.02 ^a		
F1 CS/Hik			774.6	34.77
<i>ct</i> ⁵⁶⁸⁷ / <i>ct</i> -GAL4			835.7	25.88
<i>ct</i> ⁵⁶⁸⁷ /TM3,Sb			802.9	26.99
<i>ct</i> ⁴¹³⁸ / <i>ct</i> -GAL4			818.6	23.24
<i>ct</i> ⁵⁶⁸⁷ /TM3, Sb			777.6	22.99
Canton S BH			830.8	36.42
Canton S TP			775.4	21.69
Canton S RD			750.4	20.26
<i>ey3.5</i> ^G	713.8	29.77	745.1	43.76
<i>ey3.5</i> ^{G>A}	737.0	21.12	791	44.49
<i>ey3.5</i> ^{Gl} / <i>Df(4)J2</i>			822.9	34.44
<i>ey3.5</i> ^{G>A}			847.5	19.61
<i>/Df(4)J2</i>				

^a Flies reared at 21°C.

STAR Methods

LEAD CONTACT AND MATERIALS AVAILABILITY

Further information and requests for resources and reagents should be directed to and will be fulfilled by the Lead Contact, Bassem Hassan (bassem.hassan@icm-institute.org). Reagents generated during this study are available upon request from the authors.

EXPERIMENTAL MODEL AND SUBJECT DETAILS

SPECIES

Drosophila melanogaster

D. melanogaster stocks were cultured on standard cornmeal diet food at 25°C except mentioned otherwise in the corresponding figure legend. Developmental stages used in each experiment are indicated in the corresponding method details section. Morphological measures on adult flies were performed on females only. The fly strains used in this study were: Canton-S^{BH} (Hassan lab); Canton-S^{TP} (Préat lab, provided by P. Callaerts); Canton-SRD (Davis lab, provided by P. Callaerts); Hikone-AS (Kyoto DGRC 103421); DGRP-208 (*D.m.* 3, Bloomington #25174); Act5C-Cas9 (Port et al., 2014) (Bloomington # 54590); *ct*-Gal4 (Pfeiffer et al., 2008) (Bloomington # 45603); *hth*^{NP5332}-Gal4 (DGRC Kyoto #104957); UAS-RNAi^{ct} (VDRC #v5687); UAS-RNAi^{ct} (VDRC #v4138); UAS-RNAi^{luc} (Bloomington #31603); *D.m.ey3.5^GGFP* (this study); *D.m.ey3.5^AGFP* (this study); *D.m.ey3.5^GmCherry* (this study); *D.m.ey3.5^AmCherry* (this study); *D.m.ey3.5^{NoCt}GFP* (this study); *D.m.ey3.5^{ConsensusCt}GFP* (this study); *ey3.5^G* (this study); *ey3.5^{G>A-1}* (this study); *ey3.5^{G>A-2}* (this study); *ey3.5^{G>A-3}* (this study); *ey3.5^{G>A-4}* (this study).

Drosophila ananassae

Isofemale *D. ananassae* stocks were cultured on standard cornmeal diet food at 21°C. Morphological measures on adult flies were performed on females only. Stock origin: Kisangani, Congo (DSSC 14024-0371.30) and Mumbai, India (DSSC 14024-0371.31).

Drosophila yakuba

D. yakuba stocks were cultured on standard cornmeal diet food at 21°C. Morphological measures on adult flies were performed on females only. Stock origin: Ivory Coast (DSSC 14021-8209.0261.00) and Liberia (Reference Genome strain DSSC 14021-0261.01).

Drosophila pseudoobscura

Isofemale *D. pseudoobscura* stocks were cultured on standard cornmeal diet food at 25°C except when mentioned otherwise in the corresponding figure legend. Morphological measures on adult flies were performed on females only. Stock origin: Catalina Island, California, USA (Cat; DSSC 14011-0121.121) and Chiracahua Mountains, Arizona, USA (DSSC 14011-0121.118).

Drosophila virilis

The isofemale *D. virilis* stock was cultured on standard cornmeal diet food at 21°C. Morphological measures on adult flies were performed on females only. Stock origin: Gikongoro, Rwanda (DSSC 15010-1051.118).

DEVELOPMENTAL STAGES

For selecting specific developmental stages, embryos were collected on grape fruit plates complemented with yeast paste changed every 2 hours. Freshly hatched L1 larvae were collected every two hours and transferred to corn meal food vials in a density-controlled fashion (20 larvae / vial). Staging was performed at 25°C. Correspondence of developmental stages between *D. mel.* and *D. pse.* was determined based on developmental transitions – larval hatching, L2 to L3

molt, pupa formation - and morphological features – embryo morphology, rows of differentiated photoreceptors in the EAD, size of the EAD.

DENSITY-CONTROLLED CULTURE CONDITIONS

Morphological measurements were performed on flies raised in density-controlled conditions: batches of 20 young females and males (2-5 days old) were put together and cultured at 25°C. They were transferred in fresh vials every 24 hrs. For each vial, the individuals eclosing during the first two days of eclosion only were used for measurements.

METHOD DETAILS

GENERATION OF REAGENTS

Constructs

Enhancer reporter constructs were generated using the Gateway Recombination Cloning Technology (ThermoFischer Scientific). *D. pse. ey3.3* and *D. mel. ey3.5* regulatory sequences were amplified respectively from *D. pse.* (from stock Cat; DSSC 14011-0121.121), Hikone-AS (for the *G*-variant) and Canton-S^{BH} (for the *A*-variant) genomic DNA (extracted using Qiagen DNeasy Blood and Tissue Kit #69504) and cloned into the Gateway pDONR221 entry vector (ThermoFischer Scientific #12536017) following the provider specifications. Primers for the enhancer amplifications are:

pEntry-ey^{3.3Pse}:

forward:GGGGACAAGTTTGTACAAAAAAGCAGGCTAAGTGGTAGTGGACTAGG and

reverse:GGGGACCACTTTGTACAAGAAAGCTGGGTCCTAGAATTTTGCTAACGC;

pEntry-ey^{3.5CSBH} and pEntry-ey^{3.5Hik}:

forward:GGGGACAAGTTTGTACAAAAAAGCAGGCTGGACTAGGCGGTATTGCT and
reverse:GGGGACCACTTTGTACAAGAAAGCTGGGTTTTGCTCACACATCCATTTG. The
 entry vectors with mutated forms of *ey3.5* enhancer, pEntry-ey^{3.5NoCt} and pEntry-ey^{3.5consensusCt}
 were generated by modifying the pEntry-ey^{3.5Hik} using primers carrying the corresponding
 mutations. These primers were (mutated nucleotides are in capital letters):

pEntry-ey^{3.5NoCt} :

forward: caataaaatggttg**CaG**tttttcgaactttcg

reverse: cgaaagttcgaaaa**CtG**ccaaccattttattg

pEntry-ey^{3.5consensusCt} :

forward: taaaatggtt**T**gaacttttcgaactttcg

reverse: gaaaaagttc**A**aaccattttattgttttc

Enhancer inserts were next transferred using Gateway recombination into mCherry- and GFP-
 expressing enhancer reporter vectors amenable to phiC31 integration –mediated transgenesis
 (Aerts et al., 2010; Quan et al., 2016).

pAWF-Cut: *ct* cDNA was kindly provided by I. Lohmann (U. Heidelberg). The full length
 cDNA was cloned, without its ATG, into a Gateway pEntry vector using the pEntr-D-TOPO kit
 (ThermoFischer Scientific K2400-20) following provider specifications. It was transferred using
 Gateway recombination into the pAFW vector (DGRC#1111), resulting in the addition of 3 x
 Flag tag coding sequence upstream *ct* cDNA.

pU6gRNA^{ey}: the following complementary phospho-oligomers were used to generate a double
 strand DNA sequence encoding the *ey* eye-enhancer guide RNA (gRNA): *forward*: phospho-
 CTTCGTCGAAAACAATAAAAATGGT; *reverse*: phospho-

AAACACCATTTTATTGTTTTTCGAC. After hybridization, the resulting double-strand DNA was cloned into the pU6-BBS1-chiRNA plasmid (Addgene #45946)(Gratz et al., 2013).

Enhancer-reporter lines

Transformant flies carrying enhancer reporter constructs were generated by BestGeneInc. All constructs were integrated at the Atp2 landing site using phiC31 recombination.

CRISPR/Cas9 engineering

For editing the *ey* eye enhancer, we injected SNP^G homozygous *D. mel.* Act5-Cas9 embryos (Port et al., 2014) with two constructs respectively encoding the guide RNA (pU6gRNA^{ey}) and the SNP^A-carrying *ey* eye enhancer sequence (pEntry-ey^{3.5CSBH}), each of them at a concentration of 500 ng/μl (Port et al., 2015). Candidates were screened using allele-specific PCR. We isolated one CRISPR modified male from which we established four CRISPR SNP^A lines. In parallel, a control line was established by mating non-injected Act-Cas9 flies following the same scheme their injected siblings. Sequencing the *ey* eye enhancer from the transformed SNP^A and of the non-injected SNP^G control stocks confirmed that they were differing only by this single nucleotide.

Allele-specific PCR

SNP^A and SNP^G alleles were detected by allele-specific PCR using a common reverse primer (Ey-R3: AGAAATATCACATGGCCGAG) and one of two specific forward primers differing by the 3' most nucleotide (either A or G) and including a mismatch (underlined) to increase binding specificity (Ey-SNP^G-F: GGAATCGAAAACAATAAAATGGCTGG; Ey-SNP^A-F: GGAATCGAAAACAATAAAATGGCTGA).

Cut-FLAG fusion protein expressing S2 cells

S2 cells cultivated at 25°C in Schneider's medium supplemented with 10% fetal calf serum were co-transfected with 2µg of pAWF-Cut and 0,2 µg of pCoBlast vector (ThermoFisher Scientific) using Effecten transfection reagent (Qiagen) according to the manufacturer's instructions (1/10 DNA-Effecten ratio). Blasticidin selection (10µg/µl) was applied three days after transfection. After one week of selection, cells were harvested, and expression of Cut-FLAG fusion protein was checked by western-blot using an anti-FLAG antibody (Sigma-Aldrich Cat# F3165). For long-term culture, cells were maintained in 2µg/µl blasticidin.

IMAGING AND IMAGE QUANTIFICATION

Image Processing

Except mentioned otherwise, all image processing was performed using Image J (versions 1.45 to 1.48)(Schneider et al., 2012).

Scanning electron microscopy

Whole flies were fixed overnight at 4°C in a 1:1 mix of 4% formaldehyde in phosphate buffer pH 7.2 and 100 % ethanol and dehydrated successively in graded ethanol series, hexamethyldisilazane (HMDS) and in a dessicator. Fly heads were mounted on specimen studs using silver paint in two distinct orientations: dorsal head up (for whole head imaging) and lateral (for ommatidia counts and measures). Samples were subsequently coated with platinum and images acquired in LEI mode with a JEOL JSM 7401F microscope at magnifications ranging from 120 (heads overviews) to 1900 times (ommatidia width) (Schneider et al., 2012).

Transmitted light and confocal microscopy

Preparations of adult heads for the acquisition of light microscopy images were acquired from non-fixed, freshly cut adult heads glued laterally on glass slides. Images were acquired using a

camera DFC295 (Leica) mounted on a DMRXA (Leica) microscope, operated via the open-source software Micro-Manager (Edelstein et al., 2014). Fluorescent preparations of embryos and imaginal discs were acquired using a Nikon A1R Eclipse Ti, a Leica TCS SP5 II or a Leica SP8 confocal microscope operated by the accompanying company software.

Measuring adult eye, face and antennae

All head and eye measurements were performed on female flies using ImageJ (Schneider et al., 2012). Adult Eye:Face ratio was expressed as E(Figure 1). Ommatidia width was measured on high magnification SEM images as the distance between one interommatidial bristle and the opposite angle of the facet. For each sample, measures of six adjacent ommatidia localized at the center of the eye were taken. To limit underestimation of the ommatidia width due to perspective projection distortion, samples were carefully oriented prior to image acquisition.

Ommatidia numbers

Ommatidia numbers were manually counted on SEM images using the Image J plugin “Cell counter”. We also developed an alternative method based on the approximation of the compound eye to an ellipse. With this method, the ommatidia number is calculated as the surface of an ellipse whose large and small axes correspond to the numbers of ommatidia along the compound eye anterior-posterior and dorso-ventral axes ($Area = \frac{\pi \cdot a \cdot b}{4}$ with a and b as the lengths of the large and small ellipse axes; Fig. S4). This method accommodates lower resolution images and does not require the use of SEM. Bland-Altman method (Bland and Altman, 1986) was used to compare the outcome of the two methods applied on a common set of SEM images. The ellipse method results in an overestimation of approximately 20 ommatidia as compared to the manual counting (bias mean = 20. 29; SD = 11. 70). Importantly, this difference is

independent of ommatidia number (Figure S2). Facet number estimation of Cut RNAi and CRISPR flies (Figures 4, 6, S5 and S6) were performed blind regarding to the genotype.

Measuring embryonic and larval EADs

Numbers of Ey-positive embryonic eye-antennal disc cells were counted manually. To measure the surface of the larval eye-antennal disc and eye progenitor field, regions of interest were selected manually using the Image J freehand selection tool. The number of mitotic pH3-positive cells was automatically counted using the Dead-Easy Mito-Glia ImageJ Plugin (Forero et al., 2010). The mitotic index was calculated as the number of mitotic cells per surface of the Eya-positive eye progenitor field.

mCherry and GFP colocalization

Protocol for pixel-based quantifications of mCherry and GFP colocalization was adapted from (Oliva et al., 2016). We used Fiji/ImageJ2/ImgLib2 (Pietzsch et al., 2012; Rueden et al., 2017; Schindelin et al., 2012) macro implemented in Jython. Raw images were imported using BioFormats library (Linkert et al., 2010). EADs were manually segmented in each stack by the user. Stack threshold levels for each channel were calculated using preselected auto-thresholding algorithms available in Fiji (Huang for both channels). Determined threshold levels were used to calculate Mander's overlap coefficient using Fiji implementation of the colocalization algorithm. Code for the macro is available on GitHub, <https://github.com/rejsmont/FijiScripts/blob/master/mColoc3D.py> (Oliva et al., 2016). The proportion of pixels expressing solely mCherry is used as a measure for GFP retraction.

BEHAVIORAL MEASURES OF VISUAL ACUITY

The experimental set-up is modified from (Buchner, 1976). It exploits the spontaneous tendency of fruit flies to adjust their trajectory to the surrounding landscape. Presented with rotating vertical black stripes, tethered flies spontaneously follow their movement. Narrowing the angular distance between the stripes beyond its resolving capacities makes the fly move in the opposite direction, due to an interference phenomenon similar to what we perceive when looking at the wheels of a starting train. It consists of two tracking balls and of two computer screens on which moving vertical black and white stripes are displayed in a window of 90° horizontal and 74° vertical extensions. The width of the stripes (spatial wavelength λ) as they move on the flat screen are adjusted such that they subtend a constant angle as seen from the fly 40 mm away of the screen. Pattern speed w is adapted to maintain the "contrast frequency" at 1 Hz. A positive optomotor response indicates the tendency of the flies to follow the direction of the movement of the stripes. Reduction of λ below the resolving power of the eye causes an inversion of the apparent direction of the movement of the stripes due to the geometrical interference between the fly's vertical columns of ommatidia and the vertical stripes and is accompanied by the inversion of the fly response towards negative values. The λ value at which the response of the fly is inverted (zero-crossing angle, $2\Delta\Phi$) provides a measure of spatial resolution (or visual acuity). Recordings of female *D. mel.* (Canton-S; n=9) and *D. pse.* (Cat; n=9) were performed simultaneously, with alternating assignments. We calculated the zero-crossing and its variance from the two average responses surrounding the zero-crossing (one positive, one negative) using linear interpolation and error propagation followed by t-test for differences between 2 means.

IMMUNOSTAININGS

Antibodies

We used the following primary antibodies: mouse anti-Ct (1:10, DHSB hybridoma supernatant 2B10, deposited by Rubin G. M.), mouse anti-Eya (1:75, DHSB hybridoma supernatant eya10H6, deposited by Benzer, S. and Bonini, N.M.), rat anti-elav (1:100, DHSB hybridoma supernatant Rat-Elav-7E8A10, deposited by Rubin G. M.), mouse anti-futsch (1:100; DHSB hybridoma supernatant 22C10 deposited by Benzer, S. and Colley, N.); rat anti-ey (1:300, received from P. Callaerts, (Halder et al., 1998)); anti-phosphorylated Histone 3 (1:1000, pSer10; Merck Millipore #382159); sheep anti-atonal (1:1000, received from A. Jarman and P. zur Lage, (Jarman et al., 1995)); mouse anti-GFP 3E6 (1:1000, Invitrogen, #A11120); rabbit anti-DsRed (1:1000, Clontech, #632496). Secondary antibodies conjugated with Alexa 488, Alexa 555 and Alexa 647 were used at 1:200 (Molecular Probes). Nuclei were counterstained using Draq-5 (1:1000 in PBS, Abcam #ab108410). All samples were mounted in Vectashield (Vector laboratories #H-1000).

Procedure

Fixation and immunostainings were performed following standard procedures as described in (Patel, 1994) (embryos) and in (Blair, 2000) (EADs). Briefly, embryos were collected from grape juice agar plates and dechorionated with bleach (sodium hypochlorite 3%). They were fixed in a 1/1 mixture of n-heptane and 3.7% formaldehyde in PBS and devitellinized with methanol. Larval and pupal mouth complexes including the EADs, brain and pharynx were dissected in cold PBS and fixed in 3.7% formaldehyde in PBS for 20 minutes, then washed in PBT (embryos: PBS tween 0,1%; L1 and L2 EADs: PBS Triton-X 0,1%; L3 EADs: PBS Triton-X 0,3%) for 2 hours. Blocking was performed 1 hour at room temperature in blocking solution (5% normal goat serum in PBT) and incubation with primary antibodies diluted in blocking solution overnight at 4°C. After 2 hours of washes, tissues were incubated 2 hours at room

temperature with the secondary antibodies diluted in blocking solution. After two hours of washes in PBT, tissues were rinsed in PBS, incubated with Draq5 (1/500 in PBS) 1 hour at room temperature or overnight at 4°C and mounted in Vectashield (Vector laboratories cat#H-1000). DAPI stainings were performed by adding DAPI in the mounting medium (final concentration 1,5 µm).

IN SILICO ANALYSIS

Genome Assemblies

All *D. mel.* genome positions refer to BDGP release 6 assembly (GCA_000001215.4) and *D. pse.* genome positions refer to genome release Dpse_3.0, Baylor College of Medicine (GCA_000001765.2).

Alignment of D.mel. D. pse. ey enhancer

Pairwise alignment of *D. pse.* and *D. mel.* intronic *ey* eye enhancers was performed with BLASTn (McGinnis and Madden, 2004)(blast.ncbi.nlm.nih.gov) as described in (Swanson et al., 2011). Namely, the following parameters were selected: “somewhat similar sequences” and the lower complexity filter was off. The sequences used for the alignment were: for *D. pse.* chrU:2,848,595-2,851,564 and for *D. mel.* chr4:707,672-710,917. The 22 % of alignment corresponds to “query coverage “in blastn output and indicates the amount of *D. mel.* intron sequence included in blocks aligned to the *D. pse* ortholog by BLASTn.

Ct binding site predictions

To predict possible Ct binding sites, the SNP surrounding region (500up and down) was scored with Cluster-Buster (Frith et al., 2003) (<https://github.com/weng-lab/cluster-buster> version, options -c0 -m3 -f5 -G0) using the 3 available *Drosophila* Ct PWMs (MA0128.1 from JASPAR

(Mathelier et al., 2014), Ct_Cell_FBgn0004198 and Ct_SOLEXA_FBgn0004198 from FlyFactorSurvey (Zhu et al., 2011) for the 5 different alleles (Reference, Hikone-AS, Canton-S, NoCt, ConsensusCt). Predicted Binding sites overlapping our SNP are shown with either their corresponding score in Figure 4 for the best scoring PWM (Ct_SOLEXA_FBgn0004198), and in Figure S5 for all PWMs. Predictions for the entire region are shown in Table S2.

Population genetics

We compiled whole genome sequencing data from multiple geographic samples collected in Africa, Europe, North America, Asia and Australia to investigate worldwide allele frequency patterns of the *eyeless* SNP at position Chr 4: 710326 in natural populations. This dataset consisted of single individual sequencing data (Campo et al., 2013; Grenier et al., 2015; Lack et al., 2015; Lack et al., 2016; Langley et al., 2012; Pool et al., 2012) and Pool-Seq data from various sources (Bastide et al., 2013; Bergland et al., 2014; Kapun et al., 2016; Orozco-terWengel et al., 2012; Reinhardt et al., 2014) (Table S2). For single individuals, we obtained genotypes of the focal SNP from the *Drosophila* Genome Nexus website (DGN; <http://www.johnpool.net/genomes.html>) and estimated allele frequencies based on the number of chromosomes carrying the A-variant for populations with at least ten sequenced individuals. For Pool-Seq datasets, we re-mapped quality-filtered raw data as described in (Kapun et al., 2016) and estimated allele frequencies based on read counts of the A-variant relative to the total coverage. To increase sequence coverage in Queensland and Tasmania, we merged libraries of multiple collections at the corresponding locations (Reinhardt et al., 2014). We further used a collection of Pool-Seq data from 48 population samples collected across Europe by the DrosEU consortium (Kapun et al., 2018) (accession number: PRJNA388788) for an in-depth analysis of spatial distribution of the A-variant. Specifically, we tested for clinal distribution along the

latitudinal and longitudinal axes by means of generalized linear models (GLMs) in *R* based on allele counts to account for the biallelic nature of the focal SNP. We further contrasted the clinality of 4: 710,326 to 21,008 putatively neutral genome-wide SNPs located in short introns (<60bp) and in distance to chromosomal inversions (Clemente and Vogl, 2012; Parsch et al., 2010). To test if the observed *p*-value from a GLM at the focal SNP deviates from neutral expectation we empirically assessed significance. We therefore generated empirical cumulative density functions (ECDF) based on the $-\log_{10}$ transformed *p*-values of all neutral SNPs and calculated the area under the ECDF confined by the $-\log_{10}$ *p*-value of the focal SNP and the upper tail of the distribution by integration. This area corresponds to the percentile of neutral SNPs with *p*-values equal or smaller than the focal SNP and thus summarizes the significance of clinality for 4:710,326 relative to genome-wide neutral estimates. We further characterized chromosome-wide patterns of genetic variation by estimating the population genetics statistics π and Tajima's *D* for all 48 samples from the DrosEU dataset using Pool-Gen (Kapun et al., 2018) with implemented corrections for Pool-Seq data (Futschik and Schlotterer, 2010; Kofler et al., 2011). At last, we tested whether very rare occurrences of the *A*-variant in Sub-Saharan Africa may be due to admixture with non-African genetic variation. We therefore used admixture probability estimates from (Lack et al., 2015) (see Table S2) to classify African lines as admixed (>10% of the autosomes admixed) or non-admixed ($\leq 10\%$ of the autosomes admixed) and compared genotype counts for admixed and non-admixed lines by means of Fisher exact tests (FET) in *R*.

ELECTROPHORETIC MOBILITY SHIFT ASSAYS

Nuclear extracts of stably transfected S2 cells expressing the Cut-FLAG fusion protein were prepared from cells pelleted and resuspended for 15 minutes at 4°C in the membrane lysis buffer

(Tris-HCl pH7,4 20mM, NaCl 10mM, MgCl₂ 3mM, DTT 0,5mM, NP40 1%, protease inhibitors). Cell extracts were centrifuged 5 minutes at 13000 RPM. Pelleted nuclei were then rinsed twice with PBS 1X and lysed for 30 minutes at 4°C in the nuclear envelope lysis buffer (Tris-HCl pH7,4 20mM, NaCl 100mM, MgCl₂ 3mM, EDTA 1mM, glycerol 10%, DTT 0,5mM, SDS 0,1%, sodium deoxycholate 0,5%, Triton X-100 1%, protease inhibitors). After centrifugation for 5 minutes at 13000 RPM, the supernatant containing the nuclear extract was recovered and stored at -80°C.

Cold Electrophoretic Mobility Shift Assays (EMSA) were performed with 8 or 16µg of nuclear extract using the LightShift Chemiluminescent EMSA kit (ThermoFisher Scientific) according to the manufacturer's instructions, with a modified binding buffer (Tris-HCl pH7,5 10mM, KCl 50mM, DTT 1mM, MgCl₂ 5mM, EDTA 1mM, Ficoll 400 5%, BSA 0,1µg/µl, NP40 0,05%, poly dI-dC 50ng/µl or Tris-HCl pH7,5 10mM, KCl 100mM, DTT 1mM, MgCl₂ 5mM, EDTA 1mM, NP40 0,05%, poly dI-dC 50ng/µl)

5'-biotinylated and unlabeled probes corresponding to the *G* and *A*-alleles of the *ey* enhancer were generated. To this goal, labeled or non-labeled complementary oligonucleotides were synthesized and hybridized. Oligonucleotide sequences are:

G-allele: 5'-ACAATAAAATGGTTGGAACCTTTTTTCGAACTTT-3'

A-allele: 5'-ACAATAAAATGGTTGAACTTTTTTCGAACTTT-3'

The binding was performed for 20 minutes at room temperature, followed by electrophoretic migration onto native 5% polyacrylamide gel in TBE 0,5X buffer. The supershift experiment was performed adding 2µg of the M2 anti-FLAG antibody (Sigma-Aldrich Cat# F3165).

QUANTIFICATION AND STATISTICAL ANALYSIS

In all experiments, sample size was determined *a priori*. Data were excluded exclusively prior to quantification based on poor image quality or inadequate developmental stage, explaining differences in sample size between groups. Except where stated otherwise, all statistical tests and charts were performed using Graphpad Prism 7 (Graphpad software Inc.). Normality of the data were systematically assessed and statistical tests selected accordingly. Details on statistical tests, sample sizes and *p* values are indicated in figure legends except where mentioned otherwise.

DATA AND CODE AVAILABILITY

Data and Code Availability Statement:

- The code for the macro used for quantification of GFP/RFP colocalization (Oliva et al., 2016) is available on GitHub at the following link:
<https://github.com/rejsmont/FijiScripts/blob/master/mColoc3D.py>
- Raw images are available upon request from the lead contact.

KEY RESOURCES TABLE

see separate Word document

REFERENCES

- Aerts, S., Quan, X.J., Claeys, A., Naval Sanchez, M., Tate, P., Yan, J., and Hassan, B.A. (2010). Robust target gene discovery through transcriptome perturbations and genome-wide enhancer predictions in *Drosophila* uncovers a regulatory basis for sensory specification. *PLoS Biol* 8, e1000435.
- Anderson, A.M., Weasner, B.M., Weasner, B.P., and Kumar, J.P. (2012). Dual transcriptional activities of SIX proteins define their roles in normal and ectopic eye development. *Development* 139, 991-1000.
- Anderson, C., Reiss, I., Zhou, C., Cho, A., Siddiqi, H., Mormann, B., Avelis, C.M., Deford, P., Bergland, A., Roberts, E., *et al.* (2017). Natural variation in stochastic photoreceptor specification and color preference in *Drosophila*. *Elife* 6.
- Arif, S., Hilbrant, M., Hopfen, C., Almudi, I., Nunes, M.D., Posnien, N., Kuncheria, L., Tanaka, K., Mitteroecker, P., Schlotterer, C., *et al.* (2013). Genetic and developmental analysis of differences in eye and face morphology between *Drosophila simulans* and *Drosophila mauritiana*. *Evolution & development* 15, 257-267.
- Ashery-Padan, R., Marquardt, T., Zhou, X., and Gruss, P. (2000). Pax6 activity in the lens primordium is required for lens formation and for correct placement of a single retina in the eye. *Genes Dev* 14, 2701-2711.
- Bastide, H., Betancourt, A., Nolte, V., Tobler, R., Stobe, P., Futschik, A., and Schlotterer, C. (2013). A genome-wide, fine-scale map of natural pigmentation variation in *Drosophila melanogaster*. *PLoS genetics* 9, e1003534.
- Bauer, T., and Kredler, M. (1993). Morphology of the compound eyes as an indicator of life-style in carabid beetles. *Canadian Journal of Zoology* 71, 799-810.
- Bergland, A.O., Behrman, E.L., O'Brien, K.R., Schmidt, P.S., and Petrov, D.A. (2014). Genomic evidence of rapid and stable adaptive oscillations over seasonal time scales in *Drosophila*. *PLoS genetics* 10, e1004775.

Bhattacharyya, S., Bailey, A.P., Bronner-Fraser, M., and Streit, A. (2004). Segregation of lens and olfactory precursors from a common territory: cell sorting and reciprocity of Dlx5 and Pax6 expression. *Developmental biology* 271, 403-414.

Blair, S.S. (2000). Imaginal discs. In *Drosophila protocols*, W. Sullivan, M. Ashburner, and R. Scott Hawley, eds. (Cold Spring Harbor, New York: Cold Spring Harbor Laboratory Press), pp. 159 - 173.

Bland, J.M., and Altman, D.G. (1986). Statistical methods for assessing agreement between two methods of clinical measurement. *Lancet* 1, 307-310.

Buchner, E. (1976). Elementary Movement Detectors in an Insect Visual-System. *Biological cybernetics* 24, 85-101.

Campi, K.L., Collins, C.E., Todd, W.D., Kaas, J., and Krubitzer, L. (2011). Comparison of area 17 cellular composition in laboratory and wild-caught rats including diurnal and nocturnal species. *Brain Behav Evol* 77, 116-130.

Campi, K.L., and Krubitzer, L. (2010). Comparative studies of diurnal and nocturnal rodents: differences in lifestyle result in alterations in cortical field size and number. *J Comp Neurol* 518, 4491-4512.

Campo, D., Lehmann, K., Fjeldsted, C., Souaiaia, T., Kao, J., and Nuzhdin, S.V. (2013). Whole-genome sequencing of two North American *Drosophila melanogaster* populations reveals genetic differentiation and positive selection. *Molecular ecology* 22, 5084-5097.

Clemente, F., and Vogl, C. (2012). Unconstrained evolution in short introns? - an analysis of genome-wide polymorphism and divergence data from *Drosophila*. *J Evol Biol* 25, 1975-1990.

Collinson, J.M., Hill, R.E., and West, J.D. (2000). Different roles for Pax6 in the optic vesicle and facial epithelium mediate early morphogenesis of the murine eye. *Development* 127, 945-956.

Colomb, J., and Brembs, B. (2014). Sub-strains of *Drosophila* Canton-S differ markedly in their locomotor behavior. *F1000Res* 3, 176.

Cowley, D.E., and Atchley, W.R. (1990). Development and Quantitative Genetics of Correlation Structure Among Body Parts of *Drosophila melanogaster*. *The American Naturalist* *135*, 242-268.

Crocker, J., Noon, E.P., and Stern, D.L. (2016). The Soft Touch: Low-Affinity Transcription Factor Binding Sites in Development and Evolution. *Curr Top Dev Biol* *117*, 455-469.

Czerny, T., Halder, G., Kloter, U., Souabni, A., Gehring, W.J., and Busslinger, M. (1999). twin of eyeless, a second Pax-6 gene of *Drosophila*, acts upstream of eyeless in the control of eye development. *Mol Cell* *3*, 297-307.

Darwin, C. (1872). *On the origin of species by means of natural selection; or, The preservation of favored races in the struggle for life*, 5th edn (New York, D. Appleton and Company).

Dyer, M.A., Martins, R., da Silva Filho, M., Muniz, J.A., Silveira, L.C., Cepko, C.L., and Finlay, B.L. (2009). Developmental sources of conservation and variation in the evolution of the primate eye. *Proceedings of the National Academy of Sciences of the United States of America* *106*, 8963-8968.

Edelstein, A.D., Tsuchida, M.A., Amodaj, N., Pinkard, H., Vale, R.D., and Stuurman, N. (2014). Advanced methods of microscope control using muManager software. *J Biol Methods* *1*.

Elzinga, R.J. (2003). *Fundamentals of entomology* (Upper Saddle River, USA: Pearson Education (US)).

Forero, M.G., Learte, A.R., Cartwright, S., and Hidalgo, A. (2010). DeadEasy Mito-Glia: automatic counting of mitotic cells and glial cells in *Drosophila*. *PloS one* *5*, e10557.

Frith, M.C., Li, M.C., and Weng, Z. (2003). Cluster-Buster: Finding dense clusters of motifs in DNA sequences. *Nucleic acids research* *31*, 3666-3668.

Futschik, A., and Schlotterer, C. (2010). The next generation of molecular markers from massively parallel sequencing of pooled DNA samples. *Genetics* *186*, 207-218.

Gaspar, P., Arif, S., Sumner-Rooney, L., Kittelmann, M., Stern, D.L., Nunes, M.D., and McGregor, A.P. (2019). Characterisation of the genetic architecture underlying eye size variation within *Drosophila melanogaster* and *Drosophila simulans*. bioRxiv 555698.

Gehring, W.J. (2014). The evolution of vision. Wiley interdisciplinary reviews Developmental biology 3, 1-40.

Gonzalez-Bellido, P.T., Wardill, T.J., and Juusola, M. (2011). Compound eyes and retinal information processing in miniature dipteran species match their specific ecological demands. Proceedings of the National Academy of Sciences of the United States of America 108, 4224-4229.

Gotz, K.G. (1964). [Optomotor studies of the visual system of several eye mutants of the fruit fly *Drosophila*]. Kybernetik 2, 77-92.

Gratz, S.J., Cummings, A.M., Nguyen, J.N., Hamm, D.C., Donohue, L.K., Harrison, M.M., Wildonger, J., and O'Connor-Giles, K.M. (2013). Genome engineering of *Drosophila* with the CRISPR RNA-guided Cas9 nuclease. Genetics 194, 1029-1035.

Grenier, J.K., Arguello, J.R., Moreira, M.C., Gottipati, S., Mohammed, J., Hackett, S.R., Boughton, R., Greenberg, A.J., and Clark, A.G. (2015). Global diversity lines - a five-continent reference panel of sequenced *Drosophila melanogaster* strains. G3 5, 593-603.

Grocott, T., Tambalo, M., and Streit, A. (2012). The peripheral sensory nervous system in the vertebrate head: a gene regulatory perspective. Developmental biology 370, 3-23.

Halder, G., Callaerts, P., Flister, S., Walldorf, U., Kloter, U., and Gehring, W.J. (1998). Eyeless initiates the expression of both sine oculis and eyes absent during *Drosophila* compound eye development. Development 125, 2181-2191.

Halder, G., Callaerts, P., and Gehring, W.J. (1995). Induction of ectopic eyes by targeted expression of the eyeless gene in *Drosophila*. Science 267, 1788-1792.

Hinaux, H., Devos, L., Blin, M., Elipot, Y., Bibliowicz, J., Alie, A., and Retaux, S. (2016). Sensory evolution in blind cavefish is driven by early embryonic events during gastrulation and neurulation. Development 143, 4521-4532.

Jarman, A.P., Sun, Y., Jan, L.Y., and Jan, Y.N. (1995). Role of the proneural gene, *atonal*, in formation of *Drosophila* chordotonal organs and photoreceptors. *Development* *121*, 2019-2030.

Kapun, M., Barron Aduriz, M.G., Staubach, F., Vieira, J., Obbard, D., Goubert, C., Rota Stabelli, O., Kankare, M., Haudry, A., Wiberg, R.A.W., *et al.* (2018). Genomic analysis of European *Drosophila* populations reveals longitudinal structure and continent-wide selection. *bioRxiv*.

Kapun, M., Fabian, D.K., Goudet, J., and Flatt, T. (2016). Genomic Evidence for Adaptive Inversion Clines in *Drosophila melanogaster*. *Molecular biology and evolution* *33*, 1317-1336.

Keeseey, I.W., Grabe, V., Gruber, L., Koerte, S., Obiero, G.F., Bolton, G., Khallaf, M.A., Kunert, G., Lavista-Llanos, S., Valenzano, D.R., *et al.* (2019). Inverse resource allocation between vision and olfaction across the genus *Drosophila*. *Nat Commun* *10*, 1162.

Kenyon, K.L., Ranade, S.S., Curtiss, J., Mlodzik, M., and Pignoni, F. (2003). Coordinating proliferation and tissue specification to promote regional identity in the *Drosophila* head. *Dev Cell* *5*, 403-414.

Kofler, R., Orozco-terWengel, P., De Maio, N., Pandey, R.V., Nolte, V., Futschik, A., Kosiol, C., and Schlotterer, C. (2011). PoPoolation: a toolbox for population genetic analysis of next generation sequencing data from pooled individuals. *PloS one* *6*, e15925.

Lack, J.B., Cardeno, C.M., Crepeau, M.W., Taylor, W., Corbett-Detig, R.B., Stevens, K.A., Langley, C.H., and Pool, J.E. (2015). The *Drosophila* genome nexus: a population genomic resource of 623 *Drosophila melanogaster* genomes, including 197 from a single ancestral range population. *Genetics* *199*, 1229-1241.

Lack, J.B., Lange, J.D., Tang, A.D., Corbett-Detig, R.B., and Pool, J.E. (2016). A Thousand Fly Genomes: An Expanded *Drosophila* Genome Nexus. *Molecular biology and evolution* *33*, 3308-3313.

Langley, C.H., Stevens, K., Cardeno, C., Lee, Y.C., Schrider, D.R., Pool, J.E., Langley, S.A., Suarez, C., Corbett-Detig, R.B., Kolaczkowski, B., *et al.* (2012). Genomic variation in natural populations of *Drosophila melanogaster*. *Genetics* *192*, 533-598.

Linkert, M., Rueden, C.T., Allan, C., Burel, J.M., Moore, W., Patterson, A., Loranger, B., Moore, J., Neves, C., Macdonald, D., *et al.* (2010). Metadata matters: access to image data in the real world. *The Journal of cell biology* *189*, 777-782.

Liu, W., Golovatch, S., Wesener, T., and Tian, M. (2017). Convergent Evolution of Unique Morphological Adaptations to a Subterranean Environment in Cave Millipedes (Diplopoda). *PloS one* *12*, e0170717.

Mathelier, A., Zhao, X., Zhang, A.W., Parcy, F., Worsley-Hunt, R., Arenillas, D.J., Buchman, S., Chen, C.Y., Chou, A., Ienasescu, H., *et al.* (2014). JASPAR 2014: an extensively expanded and updated open-access database of transcription factor binding profiles. *Nucleic acids research* *42*, D142-147.

McGinnis, S., and Madden, T.L. (2004). BLAST: at the core of a powerful and diverse set of sequence analysis tools. *Nucleic acids research* *32*, W20-25.

Norry, F.M., and Gomez, F.H. (2017). Quantitative Trait Loci and Antagonistic Associations for Two Developmentally Related Traits in the *Drosophila* Head. *J Insect Sci* *17*.

Nummela, S., Pihlstrom, H., Puolamaki, K., Fortelius, M., Hemila, S., and Reuter, T. (2013). Exploring the mammalian sensory space: co-operations and trade-offs among senses. *J Comp Physiol A Neuroethol Sens Neural Behav Physiol* *199*, 1077-1092.

Obbard, D.J., Maclennan, J., Kim, K.W., Rambaut, A., O'Grady, P.M., and Jiggins, F.M. (2012). Estimating divergence dates and substitution rates in the *Drosophila* phylogeny. *Mol Biol Evol* *29*, 3459-3473.

Oliva, C., Soldano, A., Mora, N., De Geest, N., Claeys, A., Erfurth, M.L., Sierralta, J., Ramaekers, A., Dascenco, D., Ejsmont, R.K., *et al.* (2016). Regulation of *Drosophila* Brain Wiring by Neuropil Interactions via a Slit-Robo-RPTP Signaling Complex. *Dev Cell* *39*, 267-278.

Orozco-terWengel, P., Kapun, M., Nolte, V., Kofler, R., Flatt, T., and Schlotterer, C. (2012). Adaptation of *Drosophila* to a novel laboratory environment reveals temporally heterogeneous trajectories of selected alleles. *Molecular ecology* *21*, 4931-4941.

Parsch, J., Novozhilov, S., Saminadin-Peter, S.S., Wong, K.M., and Andolfatto, P. (2010). On the utility of short intron sequences as a reference for the detection of positive and negative selection in *Drosophila*. *Molecular biology and evolution* 27, 1226-1234.

Partha, R., Chauhan, B.K., Ferreira, Z., Robinson, J.D., Lathrop, K., Nischal, K.K., Chikina, M., and Clark, N.L. (2017). Subterranean mammals show convergent regression in ocular genes and enhancers, along with adaptation to tunneling. *Elife* 6.

Patel, N.H. (1994). Imaging neuronal subsets and other cell types in whole mount *Drosophila* embryos and larvae using antibody probes. In *Drosophila melanogaster: practical uses in cell biology*, L.S.B. Goldstein, and E. Fyrberg, eds. (New York: Academic Press).

Pfeiffer, B.D., Jenett, A., Hammonds, A.S., Ngo, T.T., Misra, S., Murphy, C., Scully, A., Carlson, J.W., Wan, K.H., Lavery, T.R., *et al.* (2008). Tools for neuroanatomy and neurogenetics in *Drosophila*. *Proceedings of the National Academy of Sciences of the United States of America* 105, 9715-9720.

Pietzsch, T., Preibisch, S., Tomancak, P., and Saalfeld, S. (2012). ImgLib2--generic image processing in Java. *Bioinformatics* 28, 3009-3011.

Pool, J.E., Corbett-Detig, R.B., Sugino, R.P., Stevens, K.A., Cardeno, C.M., Crepeau, M.W., Duchon, P., Emerson, J.J., Saelao, P., Begun, D.J., *et al.* (2012). Population Genomics of sub-saharan *Drosophila melanogaster*: African diversity and non-African admixture. *PLoS genetics* 8, e1003080.

Port, F., Chen, H.M., Lee, T., and Bullock, S.L. (2014). Optimized CRISPR/Cas tools for efficient germline and somatic genome engineering in *Drosophila*. *Proceedings of the National Academy of Sciences of the United States of America* 111, E2967-2976.

Port, F., Muschalik, N., and Bullock, S.L. (2015). Systematic Evaluation of *Drosophila* CRISPR Tools Reveals Safe and Robust Alternatives to Autonomous Gene Drives in Basic Research. *G3 (Bethesda)* 5, 1493-1502.

Posnien, N., Hopfen, C., Hilbrant, M., Ramos-Womack, M., Murat, S., Schonauer, A., Herbert, S.L., Nunes, M.D., Arif, S., Breuker, C.J., *et al.* (2012). Evolution of eye morphology and rhodopsin expression in the *Drosophila melanogaster* species subgroup. *PLoS One* 7, e37346.

Protas, M., and Jeffery, W.R. (2012). Evolution and development in cave animals: from fish to crustaceans. *Wiley interdisciplinary reviews Developmental biology* 1, 823-845.

Quan, X.J., Yuan, L., Tiberi, L., Claeys, A., De Geest, N., Yan, J., van der Kant, R., Xie, W.R., Klisch, T.J., Shymkowitz, J., *et al.* (2016). Post-translational Control of the Temporal Dynamics of Transcription Factor Activity Regulates Neurogenesis. *Cell* 164, 460-475.

Quinn, J.C., West, J.D., and Hill, R.E. (1996). Multiple functions for Pax6 in mouse eye and nasal development. *Genes Dev* 10, 435-446.

Reinhardt, J.A., Kolaczowski, B., Jones, C.D., Begun, D.J., and Kern, A.D. (2014). Parallel geographic variation in *Drosophila melanogaster*. *Genetics* 197, 361-373.

Retaux, S., and Casane, D. (2013). Evolution of eye development in the darkness of caves: adaptation, drift, or both? *Evodevo* 4, 26.

Riska, B. (1986). Some Models for Development, Growth, and Morphometric Correlation. *Evolution* 40, 1303-1311.

Roignant, J.Y., and Treisman, J.E. (2009). Pattern formation in the *Drosophila* eye disc. *The International journal of developmental biology* 53, 795-804.

Rowan, S., Siggers, T., Lachke, S.A., Yue, Y., Bulyk, M.L., and Maas, R.L. (2010). Precise temporal control of the eye regulatory gene Pax6 via enhancer-binding site affinity. *Genes Dev* 24, 980-985.

Rueden, C.T., Schindelin, J., Hiner, M.C., DeZonia, B.E., Walter, A.E., Arena, E.T., and Eliceiri, K.W. (2017). ImageJ2: ImageJ for the next generation of scientific image data. *BMC Bioinformatics* 18, 529.

Schindelin, J., Arganda-Carreras, I., Frise, E., Kaynig, V., Longair, M., Pietzsch, T., Preibisch, S., Rueden, C., Saalfeld, S., Schmid, B., *et al.* (2012). Fiji: an open-source platform for biological-image analysis. *Nature methods* 9, 676-682.

Schneider, C.A., Rasband, W.S., and Eliceiri, K.W. (2012). NIH Image to ImageJ: 25 years of image analysis. *Nat Methods* 9, 671-675.

Singh, S., and Groves, A.K. (2016). The molecular basis of craniofacial placode development. *Wiley interdisciplinary reviews Developmental biology* 5, 363-376.

Slatkin, M. (1987). Quantitative Genetics of Heterochrony. *Evolution* 41, 799-811.

Stanger-Hall, K.F., Sander Lower, S.E., Lindberg, L., Hopkins, A., Pallansch, J., and Hall, D.W. (2018). The evolution of sexual signal modes and associated sensor morphology in fireflies (Lampyridae, Coleoptera). *Proc Biol Sci* 285.

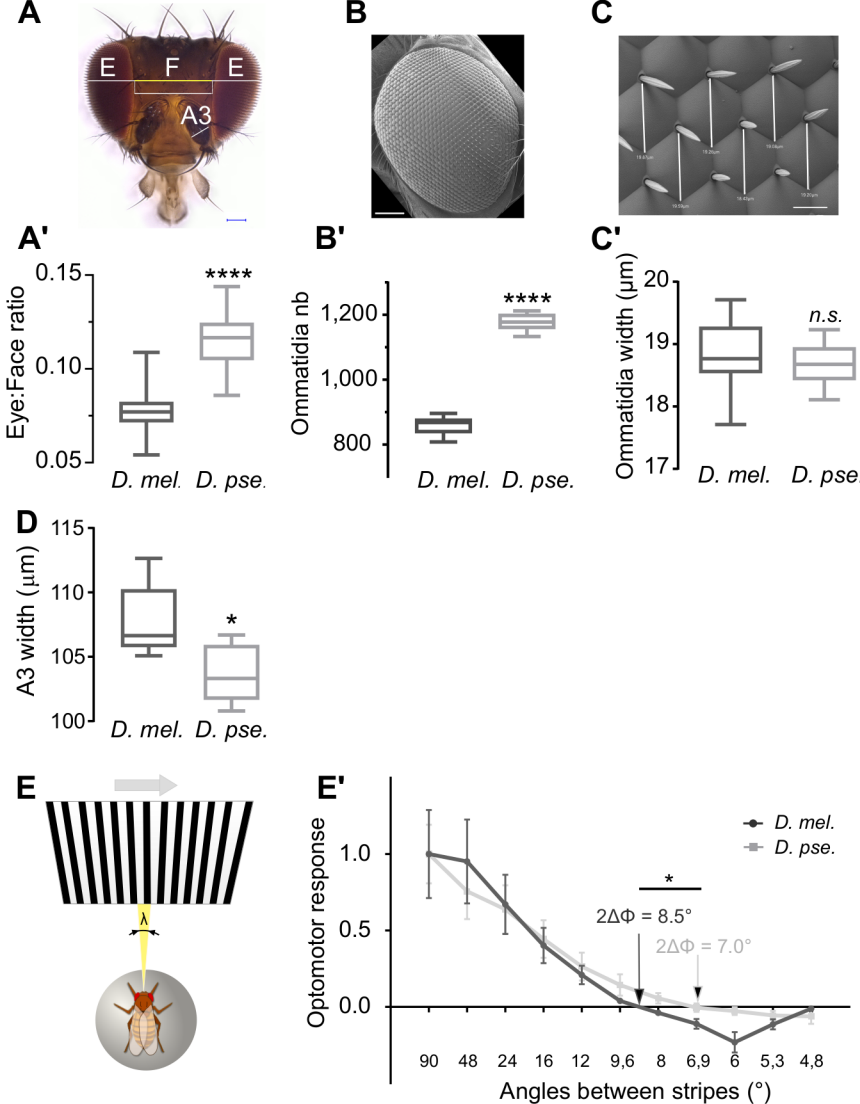
Swanson, C.I., Schwimmer, D.B., and Barolo, S. (2011). Rapid evolutionary rewiring of a structurally constrained eye enhancer. *Current biology : CB* 21, 1186-1196.

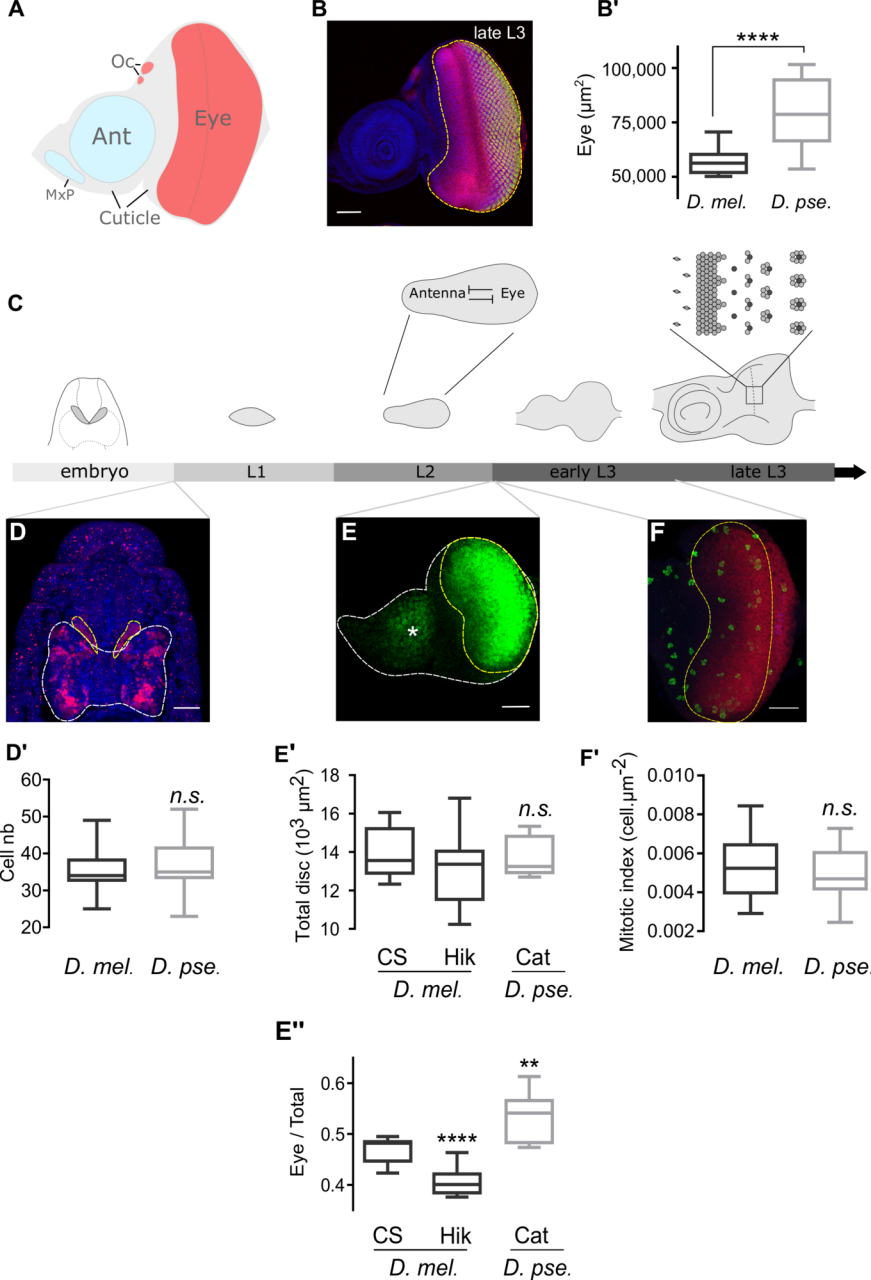
Wang, C.W., and Sun, Y.H. (2012). Segregation of eye and antenna fates maintained by mutual antagonism in *Drosophila*. *Development* 139, 3413-3421.

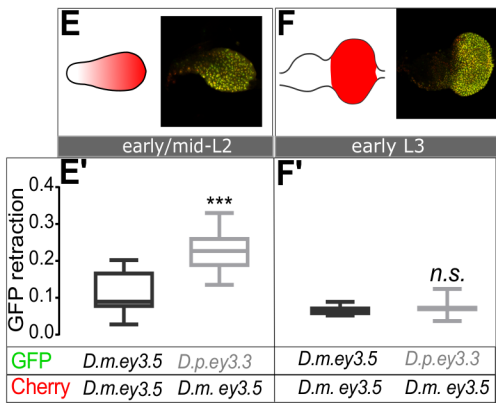
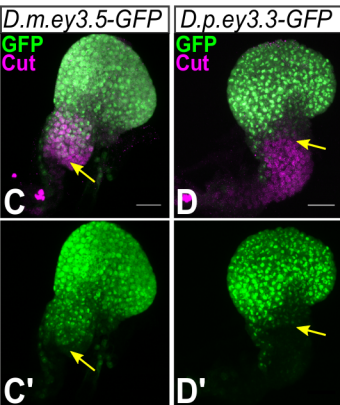
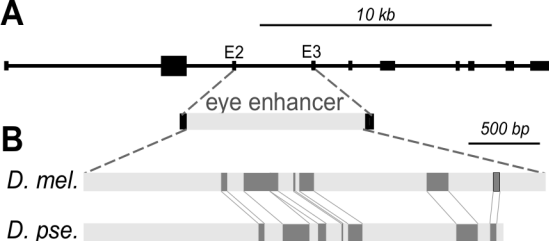
Weasner, B.M., and Kumar, J.P. (2013). Competition among gene regulatory networks imposes order within the eye-antennal disc of *Drosophila*. *Development* 140, 205-215.

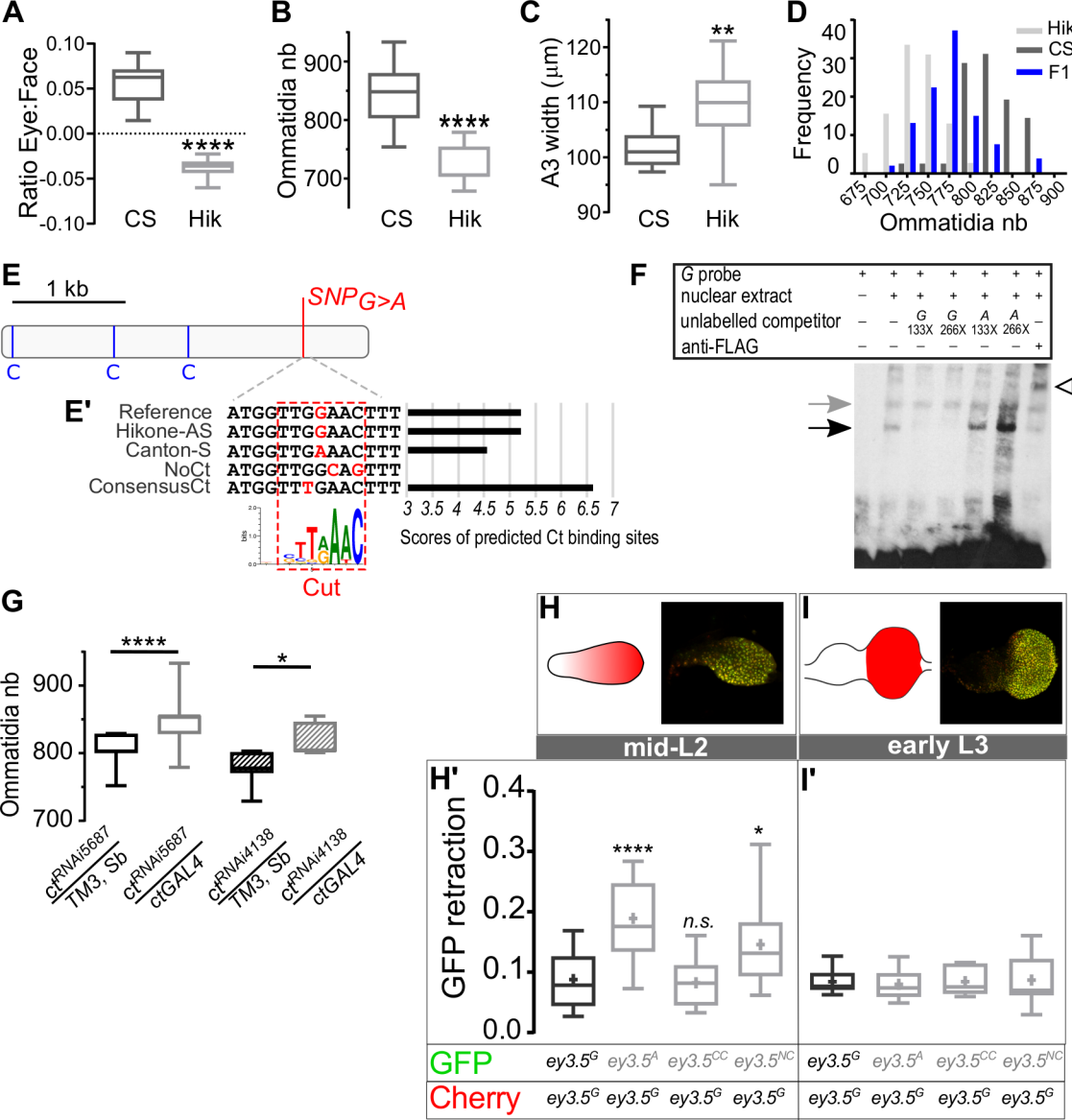
Zhu, J., Palliyil, S., Ran, C., and Kumar, J.P. (2017). *Drosophila* Pax6 promotes development of the entire eye-antennal disc, thereby ensuring proper adult head formation. *Proc Natl Acad Sci U S A* 114, 5846-5853.

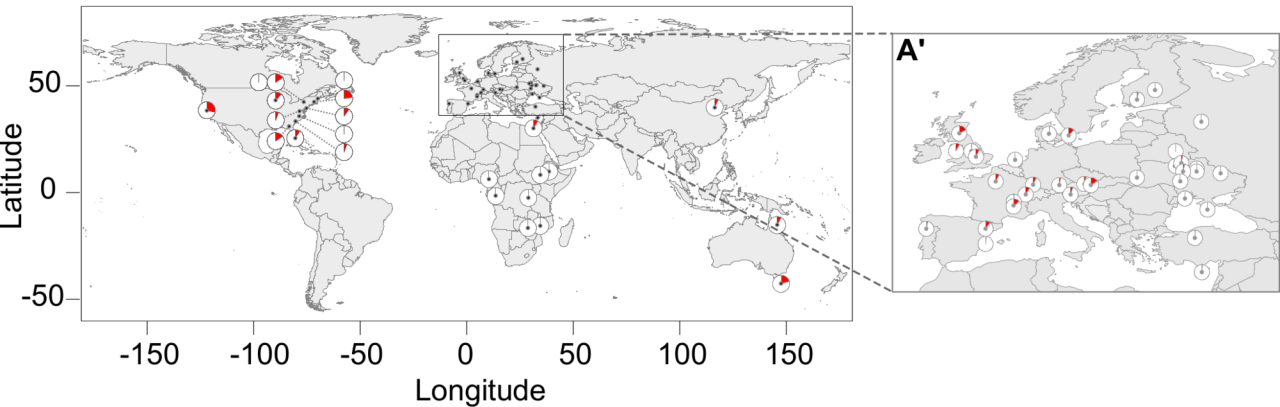
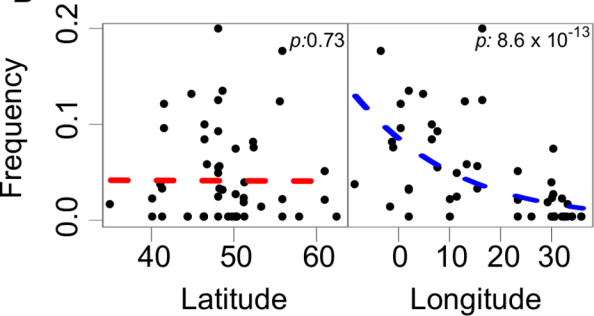
Zhu, L.J., Christensen, R.G., Kazemian, M., Hull, C.J., Enuameh, M.S., Basciotta, M.D., Brasefield, J.A., Zhu, C., Asriyan, Y., Lapointe, D.S., *et al.* (2011). FlyFactorSurvey: a database of *Drosophila* transcription factor binding specificities determined using the bacterial one-hybrid system. *Nucleic acids research* 39, D111-117.









A**B****C**